Local earthquake tomography of the Alpine region from 24 years of data

Journal Article

Author(s):
Bagagli, Matteo; Molinari, Irene; Diehl, Tobias; Kissling, Eduard

Publication date:
2025-04

Permanent link:
https://doi.org/https://doi.org/10.3929/ethz-b-000724940

Originally published in:
Geophysical Journal International 241(1), https://doi.org/10.1093/gji/ggaf028

Funding acknowledgement:
- SWISS-AlpArray - Assessing Alpine Orogeny in 4D-space-time Frame ()

Geophysical Journal International

Geophys. J. Int. (2025) **241,** 454–473
https://doi.org/10.1093/gji/ggaf028
Advance Access publication 2025 January 30
GJI Seismology

Local earthquake tomography of the Alpine region from 24 years of data

M. Bagagli ,[1] I. Molinari ,[2] T. Diehl [3] and E. Kissling [4]

[1]*Dipartimento Scienze della Terra, Università di Pisa,* I-56126 *Pisa, Italy. E-mail: matteo.bagagli@dst.unipi.it*
[2]*Istituto Nazionale di Geofisica e Vulcanologia, Sezione di Bologna,* I-40127 *Bologna, Italy. E-mail: irene.molinari@ingv.it*
[3]*Swiss Seismological Service, ETH Zürich,* CH-8006 *Zürich, Switzerland*
[4]*Institute of Geophysics, Department of Earth and Planetary Sciences, ETH Zürich,* CH-8006 *Zürich, Switzerland*

Accepted 2025 January 16. Received 2024 November 8; in original form 2024 July 19

SUMMARY

We present a new 3-D crustal *P*-wave velocity (V_P) model for the greater Alpine region (GAR). We use and merge three different high-quality datasets for local earthquake tomography covering 24 yrs, starting from 1st January 1996, up to 31st December 2019. We processed and repicked the waveforms from the events reported by the European–Mediterranean Seismological Centre with $M > 3.0$ inside the greater Alpine region for the period between May 2007 and December 2015 using a recently developed automated arrival time-picking procedure (ADAPT framework). This allows bridging the data gap between previously published (pre-2007) datasets and the recently published AlpArray research seismicity catalogue and thus provides a high-quality, highly consistent set of *P*-wave arrival times covering 24 yrs. With this dataset we derived a new minimum 1-D V_P model and associated station delays covering the entire GAR. Subsequently, we performed a series of local-earthquake-tomography (LET) inversions obtaining a 3-D V_P model with a horizontal node spacing of 20×20 km and between 7 and 15 km variable vertical spacing in the well-resolved area of investigation, thus improving the spatial and uniformly high-resolution coverage compared to previous LET studies in the area. For well-known major crustal structures, such as, for example, the geophysical Ivrea body, deep foreland basins and main orogenic crustal roots, our tomographic results correlate well with features documented by various previous seismic studies in the region. This correlation increases our confidence in the model's accuracy throughout the well-resolved area. Additionally, our model reveals previously poorly known, or unknown crustal features and it documents details in the Moho topography throughout the region. Eventually, we present a LET-Moho map (V_P isoline of 7.25 km s^{-1}) for the GAR with spatially nearly uniform resolution and document its comparison with previously published Moho maps. The new regional 3-D V_P crustal model also correlates well with a previously published V_S crustal model obtained by ambient noise tomography. These comparisons document the new LET results of combined 3-D V_P crustal velocities and Moho topography being intrinsically consistent and reliable within the region of high resolution. Hence, in addition to further improving our understanding of crustal structure geometries in the GAR, our results also provide pivotal information for a future reference seismic 3-D crustal model of the region.

Key words: Crustal imaging; Moho depth; Seismic tomography; Crustal structure.

1 INTRODUCTION

The Alps and their surrounding regions arguably are among the most widely studied and tectonically complex areas in Europe (Paul 2022 and references therein). Together with the northern Apennines, the northern Dinarides and the Carpathians orogen belts, they form the so-called greater Alpine region (GAR; see Fig. 1, black contour line as defined in Hetényi *et al.* 2018b). The close vicinity of oceanic basins and platforms to these orogenic belts leads to remarkably strong lateral crustal variations at local and regional scales (Fig. 1).

The four orogens Alps, Apennines, Carpathians and Dinarides share a common geodynamic setting (Faccenna *et al.* 2014). The general convergence of the two big plates Europe and Africa, with the Adria microplate between them, started in the Cretaceous and

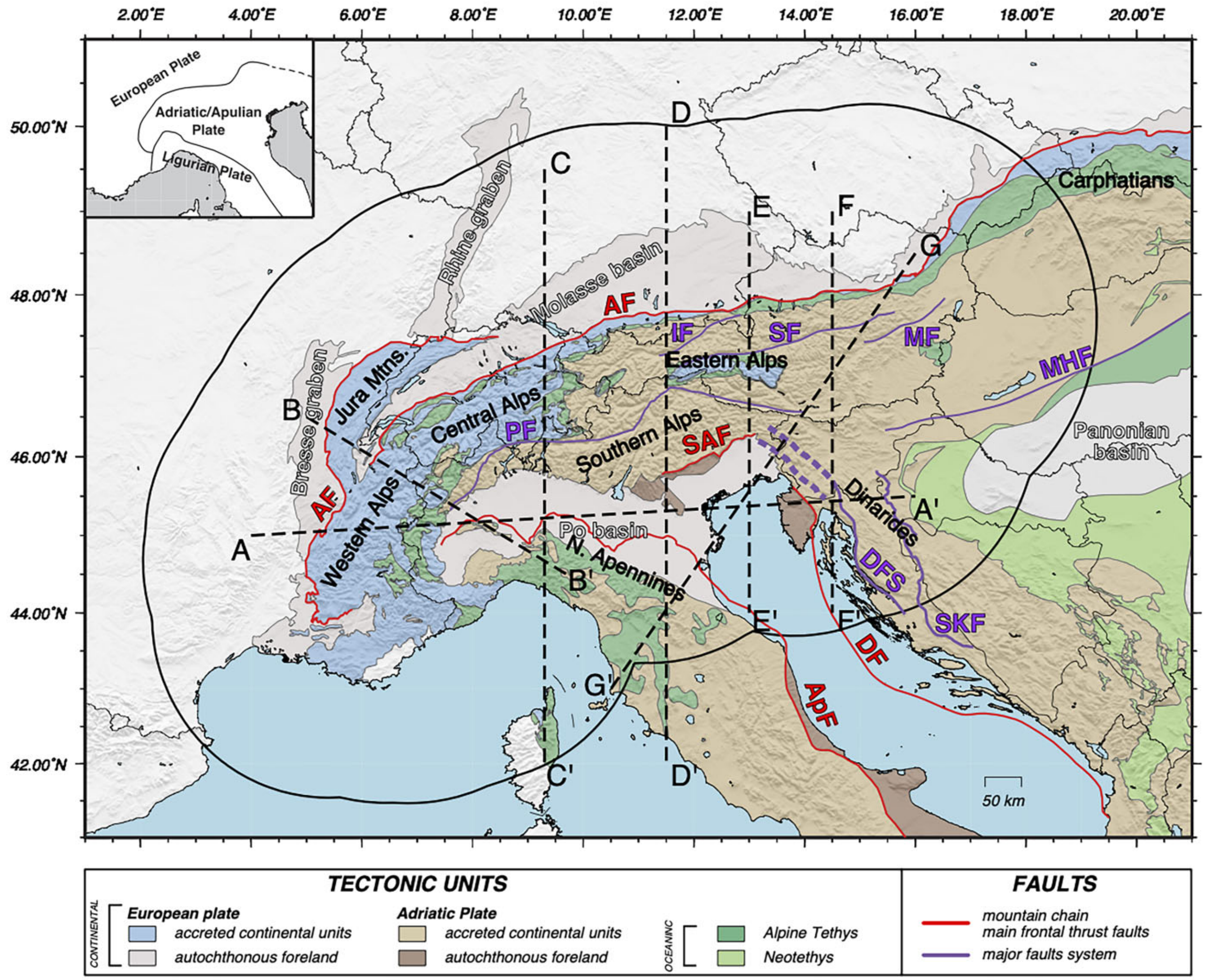

Figure 1. Tectonic map of the study region. The black contour line delimits the greater Alpine region (GAR, as defined by Hetényi *et al.* 2018b) and delimits the study area. The mountain chains' main frontal thrust fault systems (red lines) and major tectonic lineaments (purple lines) are simplified from Schmid *et al.* (2004, 2008), Handy *et al.* (2010) and Kaestle *et al.* (2020): AF: Alpine main frontal thrust fault, SAF: southern Alpine main frontal thrust fault; ApF: Apenninic main frontal thrust fault; DF: northwestern Dinarides main frontal thrust fault (Handy *et al.* 2010). PF: Periadriatic fault system; IF: Inntal fault (Reiter *et al.* 2003, and reference therein), SF: SEMP (Salzach-Ennstal-Mariazell-Puchberg) fault (Rosenberg & Schneider 2008; Frost *et al.* 2009 and references therein), MF: Mur-Mürztal faults system (Lenhardt *et al.* 2007), MHF: Mid-Hungarian faults system (Csontos & Nagymarosy 1998), SKF: Split-Karlovac transpressive zone (Chorowicz 1970), DFS: Dinaric faults system (Schmid *et al.* 2004) where NE dashed branch represent the Idrija fault and the NW dashed branch represent the Rasa fault (Grützner *et al.* 2021). Locations of the profiles presented in Fig. 6 are displayed as black dashed lines. The microplates' boundaries are represented in the inset map in the upper-left corner.

continued through the Tertiary until recent times (Trümpy 1960; Frisch 1979; Tricart 1984; Haas *et al.* 1995; Schmid *et al.* 2004; Handy *et al.* 2010, and references therein). This long period of convergence was accompanied by the opening and subsequent consumption of various ocean basins (e.g. Doglioni *et al.* 1997; Jolivet *et al.* 2009), often through rollback subduction mechanisms (e.g. Royden & Burchfield 1989; Faccenna *et al.* 2004; Spakman & Wortel 2004; Brun & Faccenna 2008), leading to the formation of a complex network of orogens either by rollback (northern Apennines, Carpathians) or collision tectonics or a combination of both (Alps, northern Dinarides) (e.g. Jolivet *et al.* 2003; Handy *et al.* 2015 and references therein).

Extensive research has been dedicated to better understanding the resulting structure and dynamics of the continent–continent collision between Adria and Europe, with numerous studies and debates during the last decades (e.g. Lippitsch *et al.* 2003; Schmid *et al.* 2008; Ustaszewski *et al.* 2008; Handy *et al.* 2010; Mitterbauer *et al.* 2011; Zhao *et al.* 2016; Kaestle *et al.* 2020; Paffrath *et al.* 2021; Nouibat *et al.* 2022; Plomerová *et al.* 2022). At crustal levels, one big plate and three microplates play a major role in the dynamics of these orogens: (i) the Tyrrhenian, (ii) the Adriatic, (iii) the Pannonian and (iv) the large European plate (inset Fig. 1). Their crustal structures have been extensively studied by the seismological and geological community (e.g. Roure *et al.* 1990; Schmid &

Kissling 2000; Carminati *et al.* 2003; Brükl *et al.* 2007; Butler 2013; Sternai *et al.* 2014; Rosenberg *et al.* 2015; Kissling & Schlunegger 2018, and references therein). With regards to regional geodynamics, and plate interaction, the Mohorovicic discontinuity (or Moho) that defines the crust–mantle boundary, is the most important lithosphere feature and, as a first-order velocity discontinuity, it is well detectable by a variety of seismic methods. Studies on crustal structure, especially Moho mapping in the GAR using active seismic surveys, began in the 1960s (e.g. Closs & Labrouste 1963) and continued for over four decades. These experiments yielded many long-range refraction profiles parallel, oblique and perpendicular to the orogen, several reflection seismic traverses across the orogen (e.g. Kissling *et al.* 2006, and references therein) and culminating in the early 2000s with a network of refraction profiles by the two experiments CELEBRATION (Guterch *et al.* 2003; Hrubcová *et al.* 2005) and ALP2002 (e.g. Behm *et al.* 2007; Sumanovac *et al.* 2009) in the eastern GAR.

Moho maps and regional crustal models of the GAR region have been published based on data obtained by different seismic methods such as receiver functions (RF) (e.g. Bianchi *et al.* 2015; Michailos *et al.* 2023; Mroczek *et al.* 2023 and references therein), surface wave (SWT) and ambient noise tomography (ANT) (e.g. Molinari *et al.* 2015; Kaestle *et al.* 2018; Lu *et al.* 2018; Qorbani *et al.* 2020; Sadeghi-Bagherabadi *et al.* 2021; Soergel *et al.* 2022; Kaestle *et al.* 2024), local earthquake tomography (LET) (e.g. Solarino *et al.* 1997; Di Stefano *et al.* 2009; Diehl *et al.* 2009a, b; Solarino *et al.* 2018; Kapuralič *et al.* 2019; Najafabadi *et al.* 2022; Menichelli *et al.* 2023; Virieux *et al.* 2023) or combining geophysical and geological information (i.e. Dezes & Ziegler 2002; Grad *et al.* 2009; Molinari & Morelli 2011). Arguably, by the combined specific seismic phases from the Moho (called PmP for the wide-angle reflection and Pn for the critically refracted wave), reversed long-range refraction seismic profiles may provide unambiguous and precise information about the crust–mantle interface like no other seismic method. Consequently, controlled-source seismology (CSS) data still denote the reliable backbone of the available information about the crustal thickness around the Earth (Prodehl & Mooney 2012; Szwillus *et al.* 2019), and the Alpine region is no exception. In general, though, the areal coverage by CSS Moho information is relatively small, and because it is obtained along profiles, 3-D migration is a pre-requisite. Therefore, good areal coverage by reliable Moho information on a regional scale may be best obtained by combining information from different seismic methods, including the CSS data (Kissling *et al.* 2006; Hrubcová & Geissler 2009; Di Stefano *et al.* 2011; Wagner *et al.* 2012; Spada *et al.* 2013).

Reliable 3-D crustal models, essential for tectonic and geodynamic interpretation, precise hypocentre locations, and seismic wavefield simulation, require detailed information on the geometries of key interfaces such as the Moho, as well as the 3-D velocity distribution. While with the RF method we obtain the best information about first-order velocity discontinuities such as the Moho, LET and ANT/SWT methods primarily provide the information about the volumetric 3-D velocity distribution. Principally, volumetric velocity and interface information often obtained by different experiments and seismic methods may be linked locally by coincident CSS information (e.g. Wagner *et al.* 2012). On a regional crustal scale, though, the combination of different seismic information yields the best results when supported by reliable LET information about the 3-D velocity distribution of both *P* and *S* waves. However, the LET method is only applicable where a significant number of distributed local earthquakes have been observed at many seismic stations. To achieve a uniformly high resolution over a large part of the GAR region this condition is met for a period of at least two decades and when observations from all permanent seismic stations operated by more than a dozen local and national observatories are combined in one single data set. Previous attempts to compile such a data set have been limited either by the noise level and inconsistencies in the data (Solarino *et al.* 1997, when only arrival-time observations were available) or by the rather short period (and reduced number of stations at the time) of available waveform data that allowed consistent repicking (e.g. Diehl *et al.* 2009a). One of the goals of the AlpArray experiment (Hetényi *et al.* 2018b) was to establish a uniform seismic waveform data base for all seismic stations operated in the region that subsequently would allow merging the local earthquake data from all permanent networks operated in the region. This task has been completed with the publication of the AlpArray Research Seismicity-Catalogue (Bagagli *et al.* 2022a).

Building on the work of Diehl *et al.* (2009a, b) and Bagagli *et al.* (2022a), the goal of this study is to provide a reliable regional-scale LET 3-D *P*-velocity (V_P) crustal model for the GAR region, exploiting 24 yrs of seismic data recorded in the region. We document how the existing arrival-time data sets were merged and extended by automated repicking procedures to extend the resolved volume in comparison to previous body wave models of the Alpine crust. The finally selected, quality-checked data set consisting of 2286 events with 84 326 first *P* arrivals has been inverted to illuminate the 3-D velocity structure of the GAR down to 60 km depth. We show that the new results correlate well with previously known structures and discuss how significantly they extend our knowledge in terms of areal coverage, precision and reliability, also by comparing the new LET model to the ANT model of Molinari *et al.* (2015).

2 COMPILATION OF ARRIVAL-TIME DATA

We compiled three different data sets spanning a total of 24 yrs (16st January 1996 – 31st December 2019) to obtain a comprehensive local earthquakes data set. In chronological order, these data sets are: (i) the one compiled by Diehl *et al.* (2009a) (referred to as DKHA data set hereafter) that was used for a previous LET in the Alpine region (Diehl *et al.* 2009b) and that covers the period January 1998 to April 2007, with observations repicked from waveforms of permanent stations of 13 national and regional observatories; (ii) a revised and fully reprocessed catalogue, compiled in this study, using waveforms from permanent observatory stations and temporary experiments openly available through the European Integrated waveform Data Archives (EIDA) for events listed in the European–Mediterranean Seismological Centre catalogue (EPOS-EMSC) between May 2007 and December 2015; (iii) the AlpArray Research Seismicity Catalogue (AARSC data set hereafter) spanning 1st January 2016 up to 31st December 2019 (Bagagli *et al.* 2022a).

2.1 Repicking the 2007 to 2019 arrival-time data of GAR

We bridge the gap of ~8.5 yrs between the two already published DKHA and AARSC data sets by (1) selecting M3+ events from the EPOS-EMSC bulletin, (2) collecting all available waveforms for these events from the EIDA data centre and (3) consistently applying the ADAPT-JHD-VELEST method (Kissling 1988; Kissling *et al.* 1994; Bagagli *et al.* 2022a, Bagagli 2022b, c). We refer the reader to the Supplementary Information (section 1, Fig. S1), where we describe the workflow and parameters used for the collection, the repicking, and the final filtering of this catalogue in detail. Additionally, we computed a revised local magnitude for each event, which is based on the final high-precision hypocentre location and re-evaluation of the amplitude observations, and a regression following the MLv scale implemented in the SeisComP software (Hanka *et al.* 2010; https://www.seiscomp.de). For a detailed description of magnitude calculations and comparisons with the original EPOS-EMSC catalogue, the reader is referred to the Supplementary Information (section 2). In this way, we provide a uniform local magnitude scale that is also consistent with the one used for the AARSC data set. Unfortunately, the magnitudes reported in DKHA have not been recalculated as most parts of the data was telemetric data, with a lot of problems (i.e. trace clipping etc.), and likely, this would have introduced more errors. Therefore, it is important to note that the uniform magnitude calculation starts from May 2007 on. This allows for a meaningful comparison of seismicity and the event-selection criteria used in tomography. The final repicked and magnitude-revised catalogue spanning from May 2007 to December 2015 consists of 1108 events with MLv ranging between 2.0 and 5.9 (Supplementary Information, section 2, Fig. S2).

2.2 Merging arrival-time data from different networks and periods

Obviously, the individual catalogues compiled by international, national and regional observatories were processed at different times, with different methods, different parameters and (most importantly) with different station coverage. The station coverage influences the network resolution and therefore the event-location accuracy (e.g. Diehl *et al.* 2021; Lee *et al.* 2023, and references therein). The station coverage between observatories not only differs but also sometimes has inconsistencies and errors in the listed station parameters. This problem is well known (e.g. Solarino *et al.* 1997; Rojo Limón *et al.* 2021, and reference therein) and may be overcome by compiling a so-called master station list (MSL). For a detailed description of the process used to establish an MSL and to recognize and handle multiple reports of station codes with different associated parameters, the reader is referred to the Supplementary Information (section 3). By application of the MSL consisting of 3091 permanent and temporary stations, we were able to correct, where needed, the station names for all 91140 observations of the 2339 events reported in the three catalogues covering the period from 1996 to 2019 (see Supplementary Information, table T1).

2.3 Minimum 1-D model as initial reference model for LET

The final step to obtain an intrinsically consistent catalogue of hypocentres and arrival times for the period 1996 to 2019, and a data set suitable for high-quality 3-D LET inversion, requires the calculation of a minimum 1-D model and corresponding station delays for the GAR using the VELEST software (Kissling 1988). This step serves the purpose to relocate all hypocentres consistently and to obtain a suitable initial reference model for the 3-D tomographic inversion (Kissling *et al.* 1994). A further reason to utilize VELEST in our analysis is to identify and eliminate inconsistencies (erroneous picks, misidentified phases, etc.) within our data set, thereby enhancing the reliability of the resulting 3-D model for interpretation (Diehl *et al.* 2009a; Husen *et al.* 2009). This process is conducted in three stages. Initially, we employ the Joint–Hypocentre–Determination (JHD) technique, using the AARSC minimum 1-D model and corresponding station delays of Bagagli *et al.* (2022a) as our initial input. This choice is strategic, as this model encompasses nearly all permanent stations, providing a robust foundation for our analysis. In this first stage, we update the merged data set's velocity model, station corrections, and hypocentre location. The second stage involves the removal of potential outlier picks, by eliminating all observations having residuals $\geq$0.6 s, as well as poorly located events, having a final azimuthal gap (gap) of $\geq 180^\circ$ or fewer than 6 *P* observations. Finally, we apply VELEST one more time in the JHD mode to obtain the final, quality-checked data set with relocated hypocentres. For the JHD inversion we use the updated 1-D velocity model and corresponding station-delay corrections obtained from the previous step. To ensure that station corrections are statistically meaningful and robust, we only consider corrections for stations with $\geq$20 *P* observations.

The results are an updated minimum 1-D model and station delays for the GAR (Fig. 2) that correspond very well with the previous 1-D model computed for the AARSC (Bagagli *et al.* 2022a). The only notable small difference between the AARSC 1-D profile and the updated one, is the slightly higher velocities in the layers between 29 and 44 km for the updated model (Fig. 2b). Also, the updated station delays agree well with the previously calculated ones (Bagagli *et al.* 2022a). They are highly consistent with the regional surface geology (Fig. 2a), documenting an overall high quality of the data set (Kissling 1988; Supplementary Information Fig. S3).

After the relocation of all events with the minimum 1-D model and station delays, we obtain an intrinsically consistent and homogeneously relocated seismicity catalogue. We applied the selection criteria of minimum number of *P* observations per event ($P_{\mathrm{obs}} \geq 6$) and maximum gap $< 180^\circ$) and selected the final data set of 2286 events with 84326 observations for the 3-D tomographic inversion (Supplementary Information table T1). The ray coverage of the final data set is displayed in Fig. 3. The estimated average picking error is 0.19 s. For details on the quality classification of arrival times, the reader is referred to the Supplementary Information (table T2).

3 TOMOGRAPHIC INVERSION METHOD

For the simultaneous inversion of hypocentre locations and 3-D V_{P} structure, we used the SIMULPS-14 code (Thurber 1983; Eberhart-Phillips 1990), with a full 3-D ray shooting algorithm (Haslinger & Kissling 2001). We defined the initial reference model based on the updated minimum 1-D model (Fig. 2b). For the 3-D model parametrization, we chose a 20×20 km horizontal node spacing for the inner region (5 km smaller than an earlier regional LET in the area; Diehl *et al.* 2009b). This spacing is stepwise enlarged in the outer regions, with spacing up to 100 km at the borders (Fig. 3). For the vertical spacing, we used a variable node gridding at depths of 2.5, 10, 20, 30, 45, 60 and 90 km (Fig. 2b).

To define the optimal number of iterations and the damping value to regularize the inversion, we performed the model-variance against data-variance test (i.e. trade-off curves), as shown in Fig. 4(a), by inverting our data set with the selected 3-D model parametrization (Fig. 3) and assessing the results for different damping values. Inversion results after five iterations for damping values d50, d70, d100 and d250 all show nearly identical final data variances with model variances varying between 0.05 and 0.09 (km/s)^2 (Fig. 4a) that are all very reasonable considering the large and structurally heterogeneous region and previous study in the area (Diehl *et al.* 2009b). To assess the effect of a higher number of iterations on the results obtained with these four damping parameters, we display

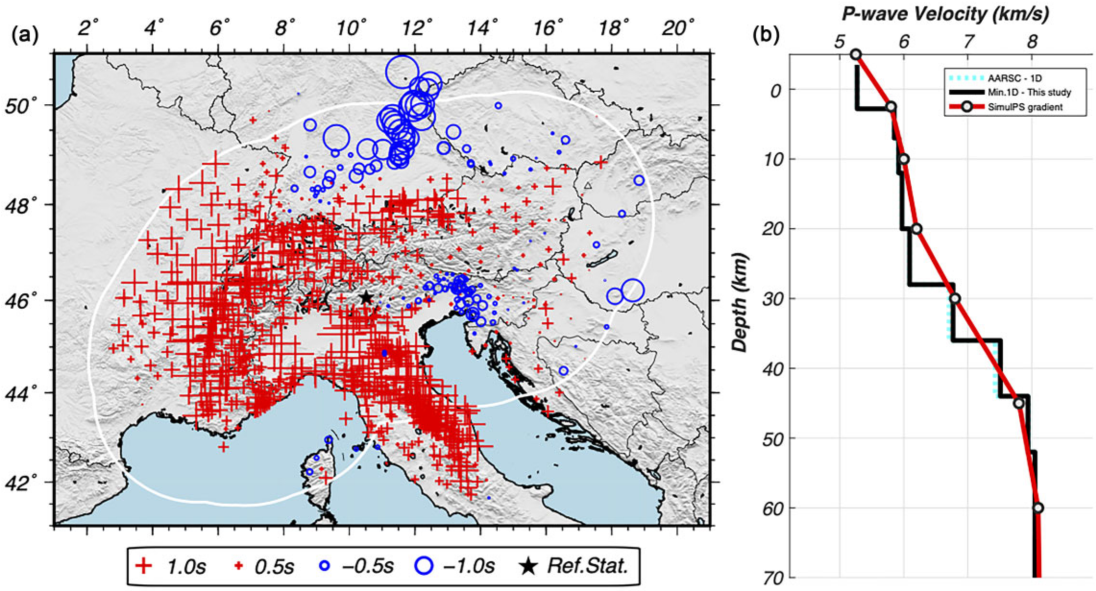

Figure 2. Updated minimum 1-D V_P model and corresponding station delays for the GAR. (a) Station delays used in this study (both permanent and temporary stations with at least 20 observations are shown). Positive delays (red crosses) indicate late arrivals and negative delays (blue circles) indicate early arrivals compared to the reference station (IV.MABI, black star). Symbol size corresponds to the amplitude of delay times. (b) 1-D V_P-depth profiles. The thick black line represents the minimum 1-D V_P model for the GAR based on the inversion of the compiled data set (this study). This model is translated into the 1-D gradient model (red line and respective grey dots), which serves as initial reference model for 3-D tomography (Kissling *et al.* 1994). Note that the updated model is nearly identical to the minimum 1-D V_P model of Bagagli *et al.* (2022a), which was computed for the AlpArray Research Seismic Catalogue (dashed light-blue line).

the RMS values versus iteration number (Fig. 4b). The final RMS values for all results remain significantly above the estimated average observation uncertainty of 0.2 s (Fig. 4b, dashed grey line). Therefore, we avoid overfitting our inversion below the data noise level. Based on these results and after cross-checking with synthetic data tests (Supplementary Information Fig. S4), we choose to use a damping value of 70 and 5 iterations.

We performed synthetic data testing, mimicking the real data set in quantity, distribution and quality, yet calculated for an *a priori* known 3-D velocity model. With such synthetic tests, we assess the solution quality and reliability of the derived tomographic model by means of standard resolution estimates [i.e. the diagonal element of the resolution matrix (RDE) for each cell] as described by Kissling *et al.* (2001). We added Gaussian random noise with a standard deviation equal to our average picking error of ± 0.2 s to the calculated (synthetic) traveltimes, which were obtained for the same source–receiver geometry as the real data. Although this procedure penalizes the (fewer) more precise, low uncertainty picks (class 0 and 1, Supplementary Information table T1), it correctly reflects most of the actual uncertainties that we have in the data set (class 2 observation, Supplementary Information table T2). Subsequently, we relocated the events using the JHD-VELEST approach with the minimum 1-D model and but with station delays set to zero (while allowing, though, their estimation during the inversion). For the inversion of the thus created synthetic data set, we use the same control parameters (initial model, parametrization, damping—unless otherwise stated, and number of iterations) as those used to obtain the results from the real data.

Initial synthetic tests with a simple model consisting of stripe-shaped anomalies (Supplementary Information Fig. S4) document the excellent recovery of amplitude and geometry of the anomalies within the region of RDE > 0.2 and good to fair recovery within the region of RDE > 0.1. To further assess the potential resolution of our data set for a more realistic earth structure, we performed a so-called characteristic model test (Haslinger *et al.* 1999). The results of this test are documented in Fig. 5 and Supplementary Information Figs S5–S6. The latter two figures show the results when a homogeneous (undisturbed) layer separates the synthetic 3-D anomalies. This setup allows for the identification of potential vertical leakage problems. From these results, we note only a downward leakage in the top 15 km of the crust but no significant upward leakage. Furthermore, Fig. 5 shows the results of a characteristic model test with 3-D velocity anomalies present in all layers down to 45 km. We note the leakage—as mentioned earlier—of the high-velocity anomaly of the 2.5 km layer into the 10 km layer (Fig. 5b).

In summary, the resolution tests document a high-quality data set, capable of resolving velocity anomalies well, with a minimum horizontal extent of 50 km (and at least 20 km wide) and an amplitude of at least 4 per cent within the region outlined by RDE > 0.2 down to a depth of 60 km. Notably, this RDE value is only slightly higher than in a previous study of the region (e.g. RDE > 0.15; Diehl *et al.* 2009b), which makes the 2 RDE-cutoffs very comparable. Based on the resolution tests, we feel confident that anomalies of large horizontal extent (>100 km) beyond the limits of RDE > 0.2 also represent real velocity structure.

4 RESULT

The results of the V_P tomography resolve the depth range from the surface to 60 km for large parts of the GAR. V_P values are presented in horizontal cross-sections as relative velocity variations with respect to the corresponding reference velocities (Fig. 6) and in a series of 7 vertical cross-sections with absolute velocities (Fig. 7).

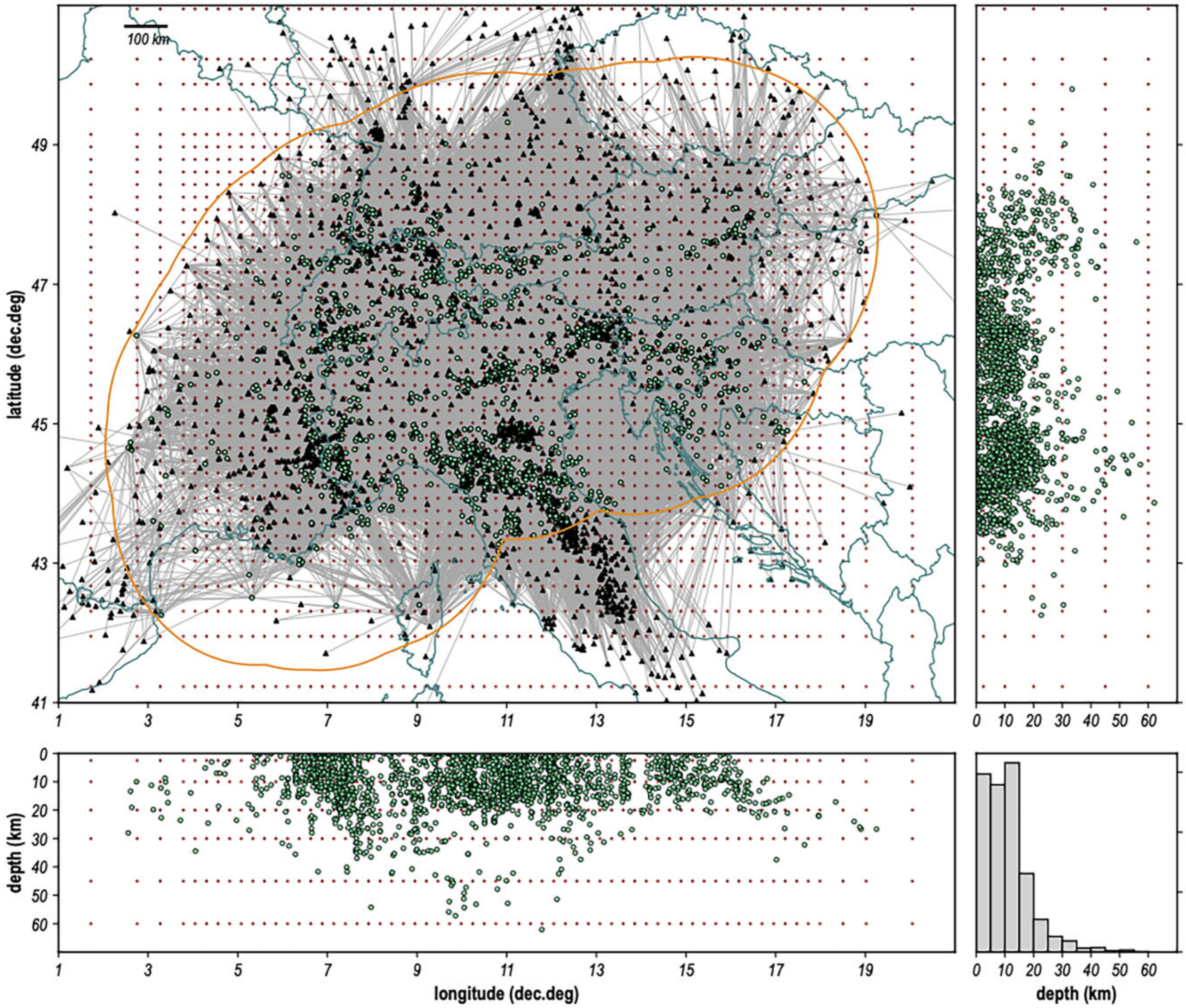

Figure 3. Hypocentre distribution of the selected well-locatable 2286 events (green circles) and the 84 326 rays (grey lines) connecting them to the 1647 stations (black triangles) used for the 3-D tomography inversion. Red crosses represent the grid nodes used for the model parametrization. We use a horizontal node spacing of 20 km by 20 km for the inner region with good cross-firing. Panel (d) document the depth distribution of the earthquakes, documenting the prevalence of upper-crustal seismicity in the Alpine region.

For clarity, we also provide the results without comments and interpretation labels in Supplementary Information Fig. S7. The solid black contour line in Fig. 6 represents the resolution diagonal element (RDE) value of 0.2, which separates the well resolved parts from the poorly to unresolved parts. Only the main orogenic fault systems are displayed for reference in Fig. 6(a). Additional geographical information can be found in Fig. 1.

In general, our tomographic results correlate very well with the large-scale crustal structure of this tectonically complex region. The velocity field of the uppermost crust (Figs 6a and b) is dominated by the thick low-velocity sediments associated with the two foreland basins, in particular, the Po basin and the Molasse basin. Note that the absence of a low-velocity anomaly in the western Po plain (visible as white spots in Figs 6a–c) do not reflect real structure but are due to insufficient ray coverage leading to low resolution as outlined in solid black. Although at the boundary of the RDE = 0.2 contour, the Upper Rhine Graben and Bresse-Rhone Graben are well-imaged as low-velocity areas (Fig. 6a). The Vienna and the Panonian basins in the east, on the other hand, appear to be beyond the limits of resolution of the data set. In the layer sensitive between 6.25 and 15 km depth (Fig. 6b), only the deepest part of the Po-basin sediments (Pieri & Gropi 1981) remains a pronounced low-velocity anomaly. Other minor low-velocity anomalies are likely due to local perturbation as no low-velocity vertical leakage from the layers directly above occurs (see the text above on resolution estimates and Supplementary Information Fig. S5). The anomaly at about 48 °N and 13 °E (though situated near the 0.2 RDE boundary), represents the deepest Molasse sediments that are reported down to 8 km depth below sea level (Hinsch 2013; Ortner *et al.* 2015). Moderately high-velocity anomalies in the depth range from surface to 6.25 km (Fig. 6a) are visible along the axis of the Alps and the northern Dinarides, where the low-velocity cover sediments have been eroded and velocities are dominated by crystalline basement rocks. The high-velocity anomaly in the northern part of the study

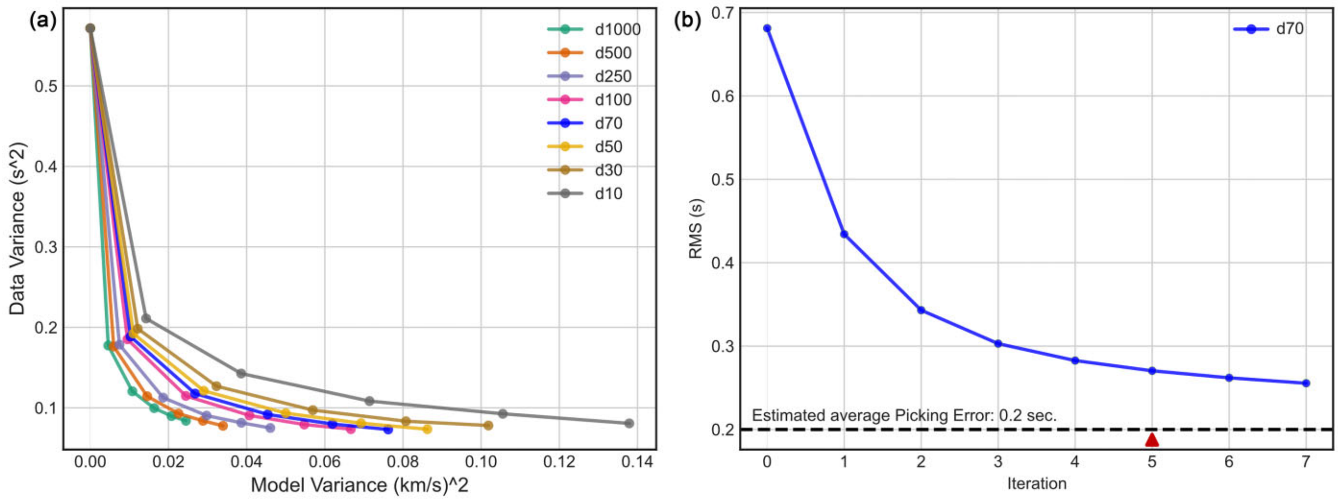

Figure 4. (a) Trade-off curves for model and data variances using different damping values. (b) Root-mean-square (RMS) fit plotted against the number of iterations used for the most relevant damping values. The final model presented here was obtained using 5 iterations and a damping value of 70. The dashed-grey line represents the estimated average pick-observation error (0.2 s).

area reaching from the SW corner of Germany to the border with the Czech Republic corresponds to the well-known (e.g. Ye *et al.* 1995), relatively high average crustal V_P beneath the Swabian Jura. As documented by the outlines of the RDE = 0.2 (Fig. 6), our data set in the upper and middle crust only resolves parts of this anomaly well. However, the relatively high-velocity anomaly beneath the Swabian Jura persists at deeper levels where the results are well-resolved between 25 and 52 km. Notably, the strongest positive velocity anomaly is visible in the depth range of 25–37.5 km (Fig. 6d), and it correlates with the Moho high of just 24 km beneath the southern Upper Rhine Graben and 26 km beneath the Swabian Jura (Kissling *et al.* 2006 and references therein).

The high-velocity of the so-called geophysical Ivrea body (Rivalenti *et al.* 1975; Ansorge *et al.* 1979; Lanza 1982; Pistone *et al.* 2020; Scarponi *et al.* 2024 and references therein) is well imaged in several layers from about 6 km depth down to 30 km depth (Fig. 6), where it connects with the uppermost mantle of Adria (Fig. 7, cross-sections A and B). Our results also document a high-velocity anomaly extending nearly latitude-parallel from the Ivrea body in the West to beneath the north shore of the Adria Sea in the East (Fig. 6d; Fig. 7, cross-sections C, D, Fig. 7 cross-section E). This ridge-type structure of the Adriatic Moho has been described based on controlled source seismology in the Moho map of Waldhauser *et al.* 1998 (their fig. 13) and in later maps based on other seismic methods (Di Stefano *et al.* 2011; Spada *et al.* 2013). From this Moho high of about 30 km depth, the Adriatic Moho descends towards SW beneath the Northern Apennines (Fig. 7, cross-section G) as documented by the more than 400 km long, relative low-velocity anomalies visible in-depth slices 20 and 30 km (Figs 6c and d, respectively). This anomaly marks the down bending of the whole Adriatic crust into the Northern-Apennines subduction (Carminati *et al.* 2003). The maximum Moho depression and thickest crustal root is in the northern part and is only about 200 km long (Fig. 6e). This geometry correlates very well with the Moho topography found by Spada *et al.* (2013).

The low-velocity anomaly representing the more than 40 km deep Alpine crustal root (Fig. 6e, Supplementary Information Fig. S7e) extends from beneath the Ivrea body at about longitude 7 °E along the inner side of the orogen arc and continues ENE-ward until about longitude 12 °E. The regions associated with yellowish colours in the depth range 37.5–52.5 km (Fig. 6e) around the two deep crustal roots of the Alps and the northernmost Apennines document the extent of the crust of about 45 km thickness. The large region with high velocities in the same depth range documents a crustal thickness of about 30 km or less as in the realm of the Swabian Jura.

5 DISCUSSION

In the following sections, we discuss and interpret selected features imaged by the new velocity model, also concerning results recently published in the literature. The discussion is based on five sites, for which 1-D profiles were extracted from our final 3-D V_P model. The selected sites (Fig. 8) are considered representative for the different geological and structural settings of the study region and include characteristics of the northern Alpine foreland (site A), the crustal root of the Alps (site B), the Ivrea body (site C), the Eastern Alps (site B), the southern Alpine foreland (site D) and the Northern Apennines (site E). For these sites, we compare the 1-D V_P profiles with the result from the V_S model of Molinari *et al.* (2015), which was obtained from an Ambient Noise Tomography (ANT), to demonstrate the resolution power of LET in terms of the Moho discontinuity. Finally, we will present and discuss a new LET-based Moho map derived from our new 3-D V_P model for the GAR and provide general comments on interpreting our LET results.

5.1 The northern Alpine foreland (site A)

The typical crustal thickness of the European foreland north and west of the Alps (Fig. 7, profiles A, B, C) is about 30 km (Waldhauser *et al.* 1998; Grad *et al.* 2009; Nouibat *et al.* 2022, their fig. 2b) with the notable local exception of the Moho highly associated with the Upper Rhine Graben region and Swabian Jura (Edel *et al.* 1975; Mueller *et al.* 1980; Di Stefano *et al.* 2011, their fig. 6) and a somewhat thicker crust beneath the Bohemian massif (Hrubcová *et al.* 2010). Based on several long-range refractions and near-vertical reflection profiles criss-crossing this region, Mueller (1977)

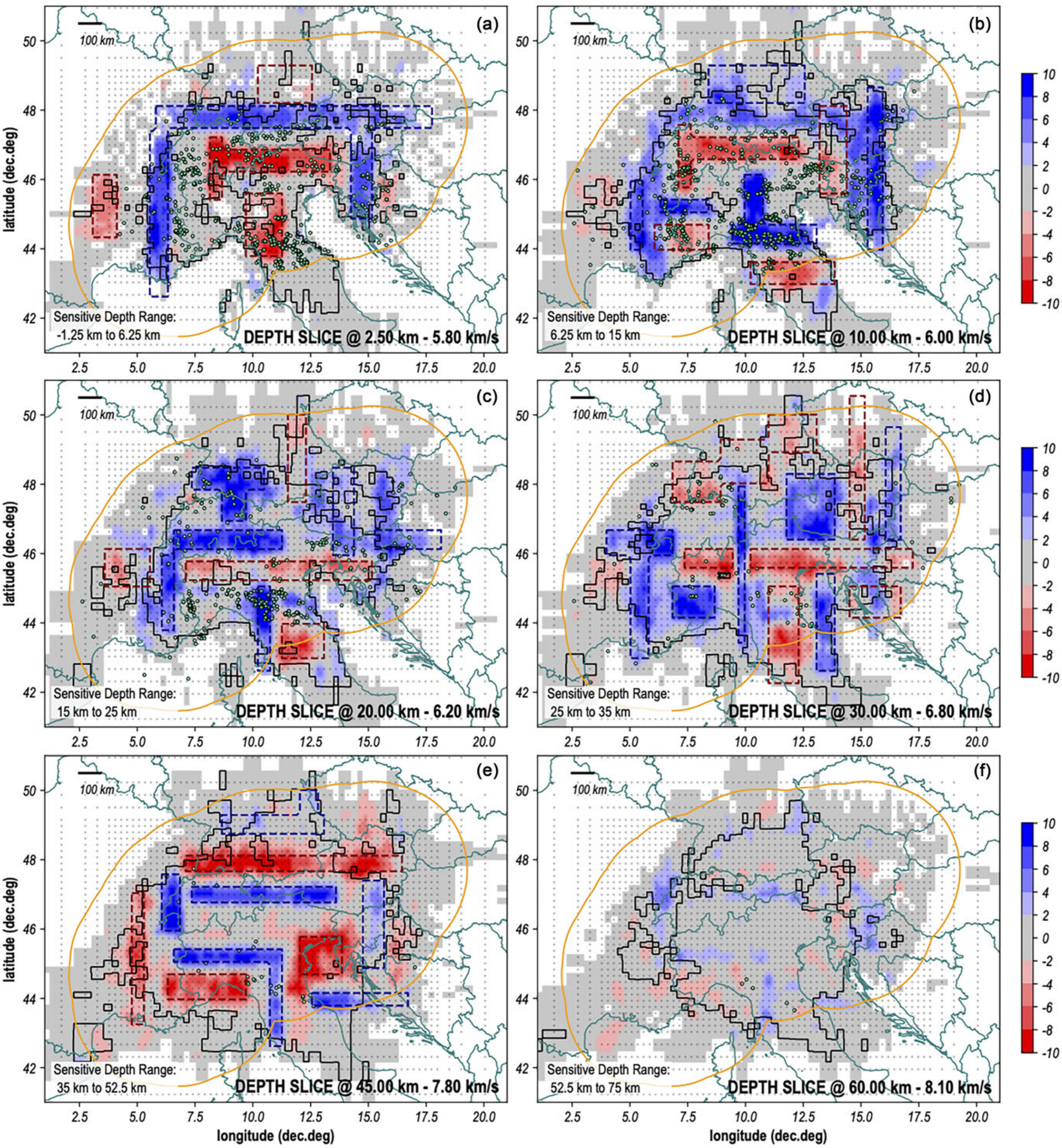

Figure 5. Results of resolution test A, using the 'characteristic model' approach (Haslinger *et al.* 1999). The model, obtained over five iterations with a damping value of 70, is depicted through horizontal depth-slices at various depths (indicated in lower right corner). To illustrate the synthetic V_P anomalies, we use blue and red rectangles to represent high (+10 per cent) and low (−10 per cent) adjustments to the reference V_P values, respectively. Earthquakes are highlighted by green circles. The RDE contour of 0.2 is highlighted by the thick black line, while grey crosses mark grid nodes. White colours indicate areas of no resolution (data gaps). The minimum 1-D V_P model reference values are specified for each layer. Additionally, the GAR region, as defined by Hetényi *et al.* (2018b), is outlined in orange.

proposed a 'new model of the continental crust' that nearly 50 yrs later, we know well, represents the 'continental crust of Variscan and Alpine Europe' (Grad *et al.* 2009, their fig. 7) with a relatively low average V_P of only 6.2 km/s in comparison with other types of continental crust (Mooney *et al.* 2002; Mooney *et al.* 2023). Beneath the Swabian Jura, however, the crustal V_P is on average 0.2 km/s higher (Ye *et al.* 1995). Our LET results (Figs 6a–c and 7, Fig. 7 profile C) confirm the earlier findings of Diehl *et al.* (2009b), and they correspond well with the locally higher V_P than normally found in the Alpine foreland. The Moho depth beneath the Swabian Jura derived from refraction-seismic surveys is about 28 km (Kissling *et al.* 2006 and references therein), and this well corresponds with

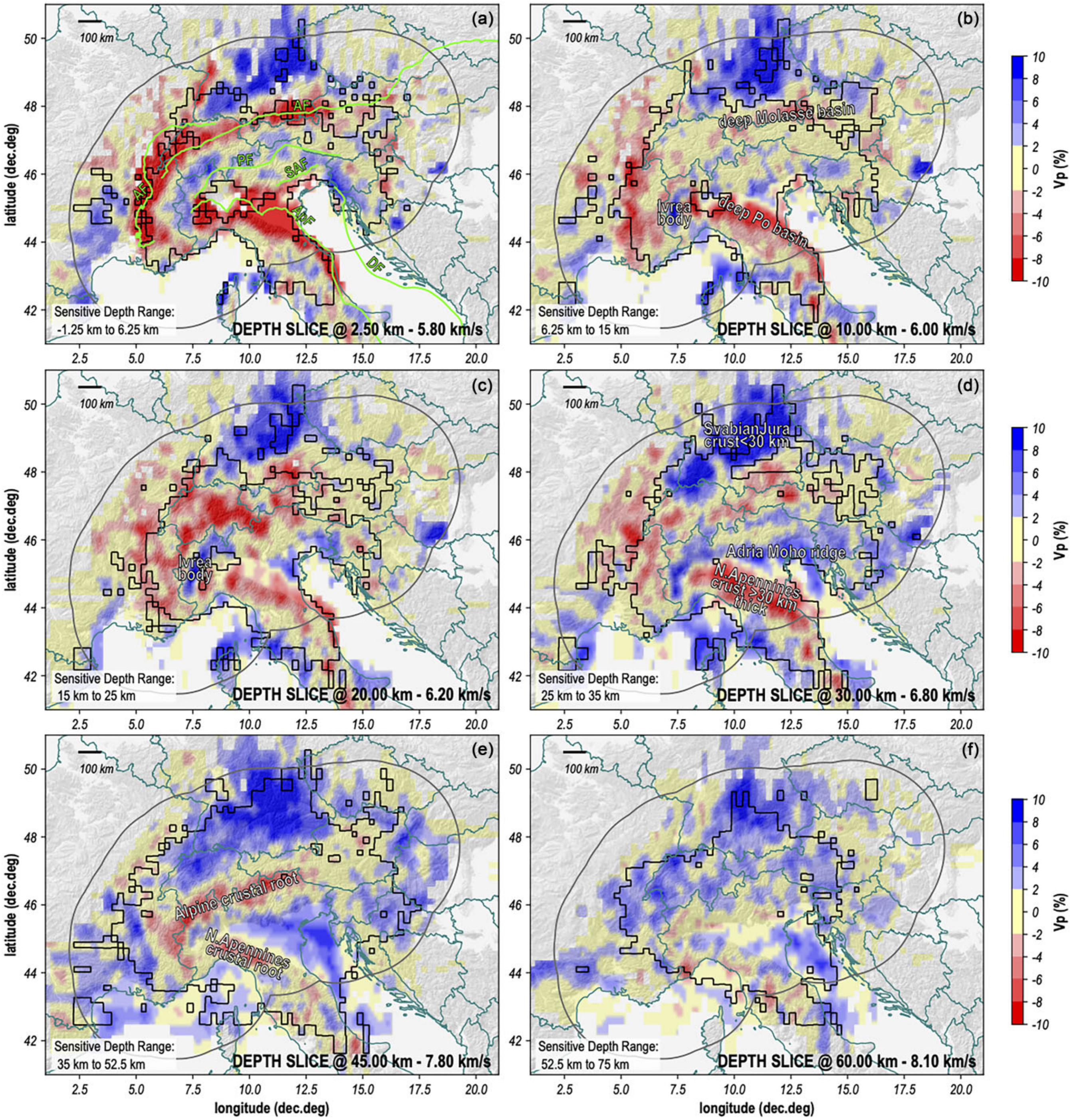

Figure 6. Horizontal slices at fixed depths of the resulting 3-D V_P model obtained using five iterations and a damping value of 70. The dark grey contour line represents the GAR region as defined by Hetényi *et al.* (2018b). The V_P velocity structure is shown as relative variation (in per cent) with respect to the 1-D initial reference model at the same depth. The black line represents the RDE = 0.2 contour, which separates the well resolved parts from the poorly to unresolved parts. The green lines in panel (a) represent the major orogen fronts and fault systems, displayed also in Fig. 1, in particular: AF, Alpine front; SAF, southern Alpine front; ApF, Apenninic front; DF, northwestern Dinarides front; PF, Periadriatic faults system.

the ambient noise tomography (ANT) *S*-velocity results presented by Molinari *et al.* (2015) and our LET results (Fig. 8, site A).

5.2 The crustal root of the Alps (site B)

The bulk of the crustal material beneath the Central Alps and the northern parts of the Western Alps are a series of stacked and thrusted units of former European origin (Roure *et al.* 1990; Blundell *et al.* 1992; Schmid *et al.* 1996). The V_P associated with the European lower crust (ELC) is, on average, 6.3 km/s (Ye *et al.* 1995). The ELC dips southwards from beneath the foreland and descends together with the mantle lithosphere down to >55 km depth into the deepest part of the Central Alpine subduction-collision zone. This translates very well in the Moho topography. Beneath the northern

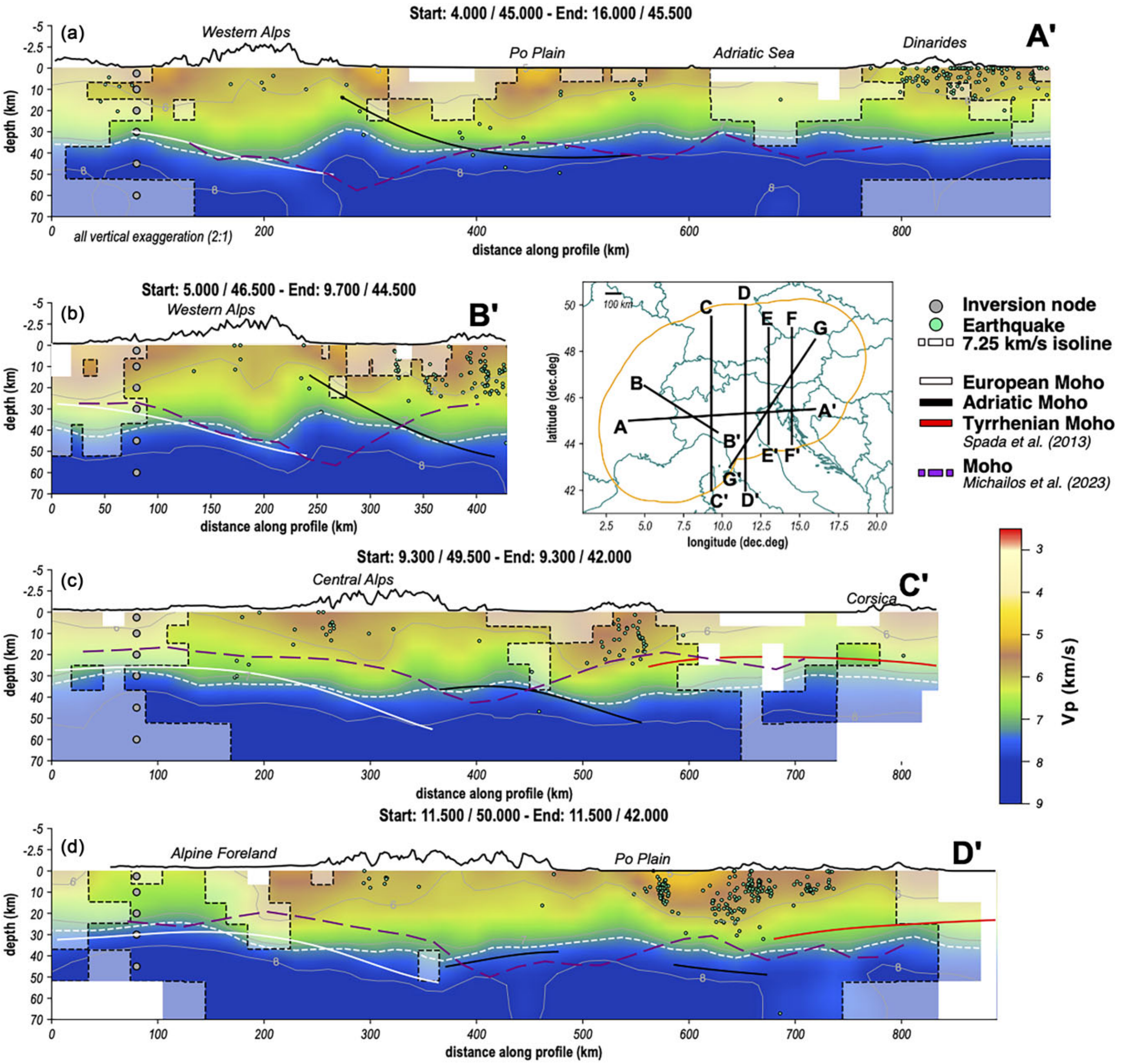

Figure 7. Vertical 2-D sections across the 3-D V_P model obtained using five iterations and a damping value of 70. Locations of all profiles are shown in the map of the figure as well as in Fig. 1. We show the absolute values of V_P. Thick dashed black lines corresponding to the RDE contour of 0.2. Regions with RDE > 0.2 are considered well resolved. Areas outside these contours are associated with fair or poor resolution and are masked accordingly (masked with transparency). The three Moho's (Tyrrhenian, Adriatic and European) as defined by Spada *et al.* (2013) and the Moho profiles of Michailos *et al.* (2023) are represented by red, black, white and purple lines, respectively. A dashed, white line indicates the 'tomographic-Moho' ($V_P = 7.25$ km/s). The light grey lines represent the velocity isolines of 5, 6, 7, 8 km/s. Only one column of inversion node is displayed at the start of each profile, to give a sense of the vertical node spacing during the inversion. All sections' profiles have a vertical exaggeration ratio of 2:1.

Alpine front, the European upper continental crust is detached from the lower crust and is imbricated, back-thrusted and uplifted (Herwegh *et al.* 2019). Since the initiation of collision at about 30 Ma, up to 20 km of upper crustal material has been removed by erosion and primarily deposited in the northern foreland Molasse basin (Schlungger & Kissling 2015). This removal left another 20 km of mainly upper crustal material on top >30 km of mostly lower continental crustal material building the orogen's crustal root (Holliger & Kisssling 1992; Fry *et al.* 2010; Diehl *et al.* 2021; this study Fig. 7 profile C). The results from this study confirm the typical European upper crustal V_P of around 6.0 km/s in the Central Alps from surface to about 20 km depth and the usual European lower crustal V_P of around 6.3 to 6.4 km/s in the crustal root below (Fig. 6). The lateral extension along the orogen of these anomalies (0% change at 10 km, −6% change at 20 km, −4% change at 30 km) documents this large-scale structure of the mountain root being representative from the Western Alpine arc through the Central Alps and into the western parts of the Eastern Alps (Fig. 7 profile D; Fig. 8, site B). Unfortunately, the resolution in the layer 15km to 25 km depth (Fig. 6c) east of longitude 12 °E is insufficient to decide on a possible

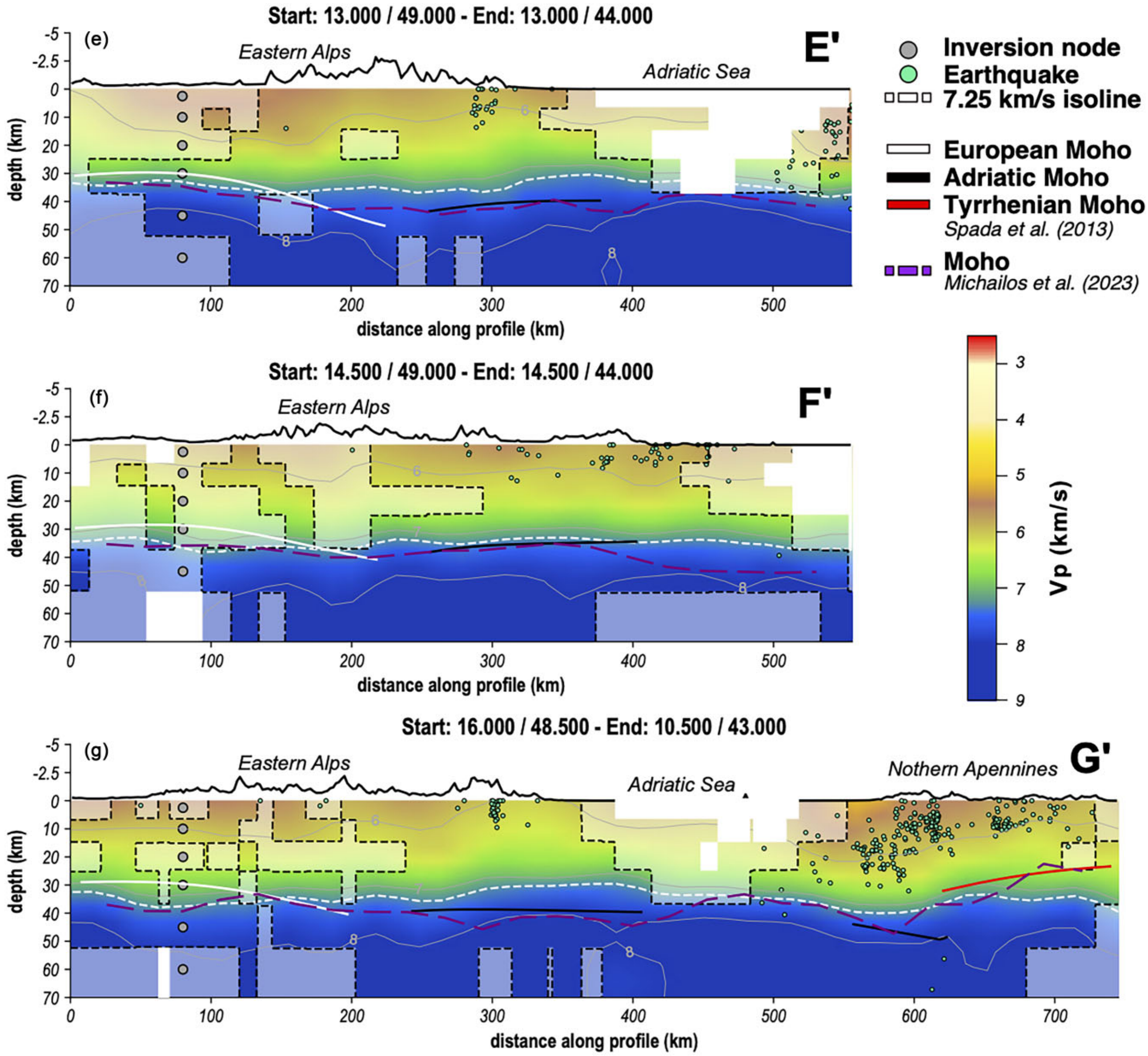

Figure 7. Continued.

continuation further along the Eastern Alps or on the thickness of the Eastern Alpine thrust sheets that comprise the top layers (Fig. 7 profiles E and F).

5.3 The Ivrea body (site C)

Along the inner arc of the Western Alps, the high-velocity Ivrea body dominates the velocity structure (Fig. 7, profiles A and B) and marks the plate boundary between Europe and Adria (e.g. Schmid *et al.* 2017 and references therein). This dominance is true for any velocity-sensitive seismic imaging method (Kissling *et al.* 2006 and references therein) and for V_P (Solarino *et al.* 1997; Paul *et al.* 2001; Diehl *et al.* 2009b; Solarino *et al.* 2018) as well as V_S (Molinari *et al.* 2015; Zhao *et al.* 2020; Nouibat *et al.* 2022; Scarponi *et al.* 2024). Thanks to the high-velocity, high-density and high-susceptibility Ivrea body, the Europe–Adria plate boundary along the Western Alpine arc is exceptionally well-defined at depth. This definition is not only due to the significant Moho offset (Fig. 7, profiles A and B), but also the velocity structure (Fig. 8, site C). While the ANT (Molinari *et al.* 2015) provides reliable volume-averaged V_S, documenting the significant volume of the Ivrea body (Adriatic lithosphere mantle) at depth below 20 km, the LET allows to differentiate between the cells west of the plate boundary showing typical European crustal (low) V_P down to at least 30 km depth, while the cells on the eastern side of the plate boundary exhibit typical Ivrea body (high) V_P shallow as 10 km depth. However, we cannot exclude even shallower depths as suggested by the ANT of Scarponi *et al.* (2024).

The deep structure of the Western Alpine arc and the Ivrea body has been the target of many seismic experiments for the past 40 yr (e.g. Paul 2022), and the recent study by Virieux *et al.* (2023) provides the opportunity to compare the results of our regional study with those of a higher resolution LET along the CIFALPS profile (Supplementary Information Fig. S8). The comparison provides a

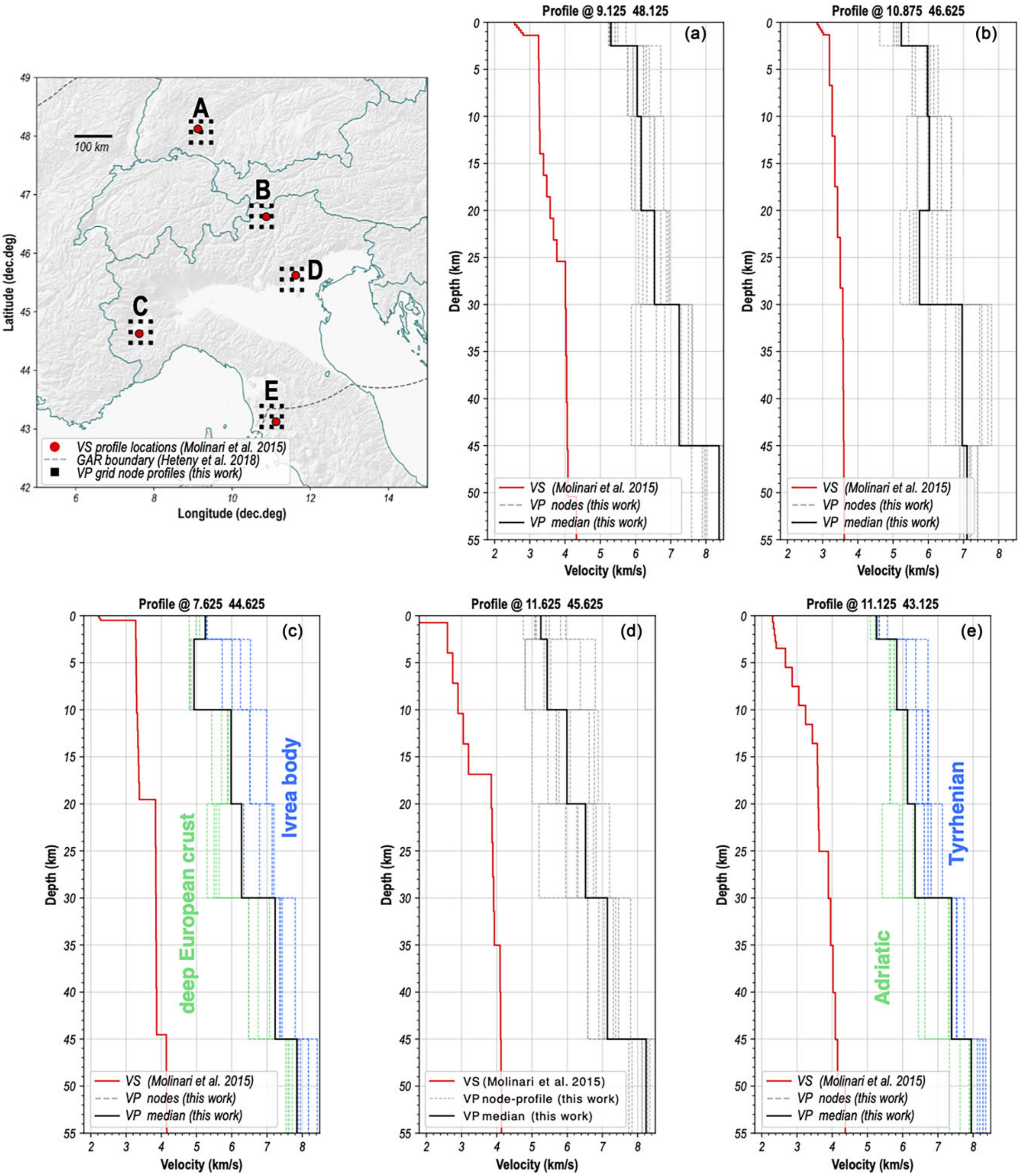

Figure 8. Velocity-depth profiles for both V_P (this work) and ANT-derived V_S (Molinari *et al.* 2015) for selected sites in the GAR. The map illustrates the locations of the 1-D profiles: red dots in the map indicate the sampling points for V_S, the black squares indicate the nine closest V_P nodes to it. In all profiles, the thick black lines represent the median of these nine V_P profiles, while the individual V_P profiles are shown as light grey lines. Thick red lines indicate the V_S profile derived from ANT. See the text for discussion and interpretation.

good example how results obtained with same method (LET in this case) and different inversion parameters for different data sets or results from different methodologies (see Paul 2022, fig. 2.3) complement each other and thus provide confidence in the main features of the structural model. The latter is documented by the excellent correspondence of the LET derived crust–mantle boundary with the CSS-derived European and Adria Moho by Spada *et al.* (2013). The finer gridding and a locally much higher number of events allow

Virieux *et al.* (2023) to reliably resolve more details, nicely illuminating the shallow parts of the suture zone beneath the Ivrea body in the Western Alps. Due to the lack of deep hypocentres beneath the Ivrea body the deeper parts of the low-velocity suture zone remain poorly resolved by LET (Solarino *et al.* 2018) but may be inferred by combining different seismic techniques, including RF (Paul 2022). By presenting several different resulting models for the CIFALPS transect, the study by Virieux *et al.* (2023) also provides great insight into the LET inversion process that requires *a priori* choice of several parameters. For the comparison with our regional model results (Supplementary Information Fig. S8) we have chosen the model by Virieux *et al.* (2023) presented in Supplementary Information Fig. S20 because they compare this model with some previously published ones.

5.4 The eastern Alps and the periadriatic fault system (Site D)

Following the AlpArray experiment (Hetényi *et al.* 2018b) the Eastern and Southern Alps have recently been the target region of several ANT and LET studies. Results from a local LET reported by Najafabadi *et al.* (2022, their fig. 10) along the TRANSALP transect document a distinctive difference in V_P in the top 20 km between the Eastern Alps north of the Periadriatic Fault System (PAFS)—that on the surface marks the plate boundary between Europe and Adria—and the Southern Alps. In the Southern Alps, the relatively low V_P of only 5.9 km/s extends to a depth below 20 km (Figs 6c and d). At shallower levels, down to about 10 km, V_P varies locally between 5.5 and 6 km/s on either side of the PAFS and this structure possibly corresponds to lateral variations in lithology of the Eastern Alpine nappes system that provides the cover unit except in the Tauern window (Schmid *et al.* 2013; Rosenberg *et al.* 2018). Significant lateral variations of V_S in the crust of the Eastern and Southern Alps based on ANT have also been reported by Qorbani *et al.* (2020). While V_P found in this study along the corresponding profile D (Fig. 7) in the top 20 km of the crust is indeed similarly low (around 6 km s^{-1}), our results do not show such a difference between north and south of the PAFS. It is likely that the resolution in our regional LET does not allow imaging of these differences, while the 450+ hypocentres located in the top 15 km of the crust used in the local LET (Najafabadi *et al.* 2022) will allow us to resolve these details. Below 20 km depth, however, thanks to the use of more distant and deeper hypocentres, the resolution in our regional LET is superior to the one of the local LET. In the depth range of 25–37.5 km (Fig. 6d), we see higher velocities beneath the Southern Alps than north of the PAFS. This may well account for the significantly thicker crustal root north of the PAFS, containing the stacked European-derived crustal material below the cover layer of the Eastern Alpine nappes. The depth profile C (Fig. 8) locates just north of the PAFS and reflects the relatively low V_P of, on average, 6 km/s with significant lateral variations down to 20 km depth with a 50 km deep crustal root on the European side and up to 6.5 km/s high lower crustal velocities and a shallower Moho on the Adria (Southern Alps) side. Interestingly, the ANT for this location (Fig. 8, site B) does reflect the relatively low-velocity deep crustal root with a Moho below 50 km depth.

5.5 The southern Alpine foreland and northern Apennines (Site D and E)

On average, the V_P structure of continental Adria (Fig. 8, site D) resembles that of the northern and western European foreland. Along the so-called Adriatic Moho ridge (Fig. 6d), located between the three orogens Alps, Apennines and Dinarides, the crust of about 30 km thickness exhibits an average V_P of about 6.2 km/s (this study Fig. 8 site D; Waldhauser *et al.* 1998; Diehl *et al.* 2009b; DiStefano *et al.* 2009). Further east, the Adriatic crust thickens below the northern Dinarides. However, according to the local LET results, it maintains an average V_P of only 6.0 km/s for the top 20 km of the crust (Kapuralič *et al.* 2019; Rajh *et al.* 2022, 2024). This top layer overlies an apparently 20 km thick lower crust. The lower crust has a V_P of either 6.5 km/s (Kapuralič *et al.* 2019) or 6.6–7.1 km/s (Sumanovac *et al.* 2009). With an unfortunate data gap across the Adriatic Sea, our results extend beyond the previous regional LET studies (Solarino *et al.* 1997; DiStefano *et al.* 2009; Diehl *et al.* 2009b) and show a 40 km thick crust (Fig. 7 profile A). In this part, V_P values of our LET model correspond to those reported by Kapuralič *et al.* (2019) and Rajh *et al.* (2022, 2024), with a maximum Moho depression beneath the northern Dinarides well agreeing with recent RF results (Stipčević *et al.* 2020).

Though largely filled by Alpine sediments, the >12 km deep Po basin evolved as the foreland basin to the Northern Apennines roll-back subduction of the Adria microplate. The downbending of the plate by the slab pull force is well documented in the basin structure and Moho topography (Carminati *et al.* 2003; Fantoni & Franciosi 2010; D'Acquisto *et al.* 2020; Pezzo *et al.* 2020) and prominently visible in our results (Figs 6d and e, Fig. 7 profile C, D, G). Compared with the regional LET by Diehl *et al.* (2009b), the data set compiled and inverted in this study allows for a reliable and continuous resolution of the Adriatic crust significantly further towards east beneath the Northern Dinarides and south beneath the Northern Apennines. While the low-velocity anomaly in the depth range 25–37.5 km (Fig. 6d) associated with the downbending of the Adriatic crust toward SW is nearly identical in its extension along the Northern Apennines with the results presented by Diehl *et al.* (2009b, their fig. 9), the extension of the deepest crustal root reaching a depth of 50 km is confined to the northernmost part (north of latitude 44 °N) (Fig. 6e). The velocity-depth functions at site E (Fig. 8) are located further south along the Adria-Tyrrhenian plate boundary. As the ANT surface waves (Molinari *et al.* 2015) preferably sample the Tyrrhenian side with the high velocities at shallow depths, the V_S depth function shows a Moho depth of about 25 km. The LET V_P median depth function, though, documents a mathematical mixture between the consistently higher V_P velocities belonging to the Tyrrhenian crust southwest of the plate boundary and the equally consistent lower V_P velocities of the Adriatic crust on the northeastern side with a Moho depth of 45 km. These velocities and the Moho topography on either side of the plate boundary correspond very well with the information obtained by LET (Di Stefano *et al.* 2009) and by RF and CSS (Di Stefano *et al.* 2011).

5.6 LET-based Moho topography of the GAR

In contrast to long-range refraction seismic with the specific and prominent PmP phase, regional LET is not specifically designed to image the first-order velocity discontinuity associated with the crust–mantle boundary (Moho). Nevertheless, regional LET provides reliable and precise information about the interface geometry and the velocities above and below the Moho. As synthetic tests document (Diehl *et al.* 2009b, their fig. 8; Wagner *et al.* 2012), in LET, with well-resolved cells of vertical dimensions not exceeding

15 km and of horizontal dimensions of 20 to 30 km, the crust–mantle boundary may be assumed as approximately being imaged by the V_P contour of 7.25 km/s. Of critical importance for continuously mapping the Moho, though, is a laterally more or less uniform resolution of the crustal velocity above and the mantle velocity below the interface (Wagner *et al.* 2012). Furthermore, the focusing and de-focusing effects of laterally extended high- and low-velocity anomalies near the Moho can impact the results. Because LET is based mainly on hypocentres located within the crust, lateral variations in the sub-Moho velocity might be artefacts. Despite this, the Moho topography's boundary is still well resolved (Diehl *et al.* 2009b, their fig. 7).

In this study, the largest region with homogeneously high resolution is obtained in the layers 30 and 45 km (Figs 6d and e). From previous studies, we expect the Moho to be located in this depth range for more than 90 per cent of the region, that is, within either one of these two well-resolved layers. Comparison of our LET results with the Moho map by Spada *et al.* (2013) based on CSS, RF and LET (Diehl *et al.* 2009b) document an excellent match (Fig. 9) within the well-resolved region. The new LET results, however, extend beyond the well-resolved region by Spada *et al.* (2013), particularly in the East. The W-E trending Moho ridge of about 30 km depth already described by Waldhauser *et al.* (1998) based on CSS data and by Stehly *et al.* (2009) based on ANT data extends all along the southern margin of the Southern Alps and widens in the East beneath Venice (Fig. 6d) from where it descends again to about 40 km depth beneath the N Dinarides (Fig. 6e). The latter structure again is in excellent agreement with published information from various seismic data sources (Sumanovac *et al.* 2009; Stipčević *et al.* 2020; Rajh *et al.* 2022, 2024).

The Moho topography beneath the Eastern Alps, particularly along the EASI transect (about longitude 13 °E), is a matter of debate. Depending on the seismic method applied and their interpretation, the deepest parts of the orogenic crustal root reach down to 70 km depth and belong to Adria (Hetényi *et al.* 2018a by RF study) or they belong to Europe and only reach down to 50 km depth (Behm 2006; Behm *et al.* 2007; Brückl *et al.* 2007; Bianchi *et al.* 2015; Bianchi *et al.* 2021). Based on an RF analysis, Mroczek *et al.* (2023, their fig. 7) suggested that the European Moho reaches a depth of 90 km along longitude 14 °E. This depth is below the Pannonian Moho depth below the Pannonian reaches the 35 km depth Mroczek *et al.* (2023, their fig. 7). Bianchi *et al.* (2021, their fig. 5) document an excellent correlation between the CSS Moho information and their global phase seismic interferometry results though the 'typical Moho signal disappears where the Moho steeply dips beneath the central parts of the Eastern Alps'. This section of the transect is characterized by strong reverberations in the middle crust both by RF imaging (Hetényi *et al.* 2018a; Michailos *et al.* 2023) and global phase seismic interferometry (Bianchi *et al.* 2021) and it is the location where by CSS (Behm 2006) and LET methods (Najafabadi *et al.* 2022, their fig. 9) a lower crustal volume of anomalously high velocity has been found. An anomalously high velocity of 7.2 km/s or higher immediately above the Moho will not only significantly reduce the amplitude of the Moho RF signal but it will also cause the PmP phase in CSS to disappear (Bleibinhaus & Gebrande 2006) and this led Spada *et al.* (2013) to propose a Moho gap between the European and the Adria Moho along plate boundary. In the same location, our LET results also document an anomalously high velocity in the lowermost crust and this locally prevents the definition of the LET Moho (Fig. 9) as the velocity gradient from typical crustal velocities to mantle velocities is not observed. Hence, our results not only correspond well with the local

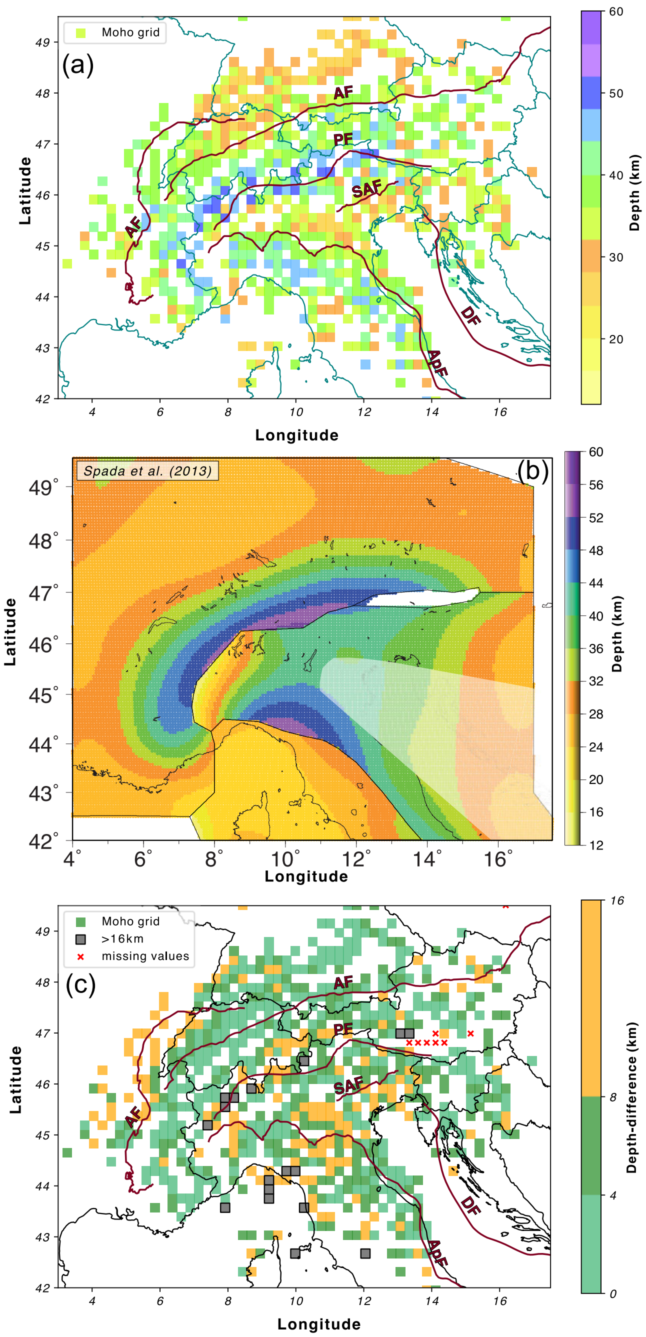

Figure 9. Mapping of the seismic V_P isoline of 7.25 km s^{-1}, interpreted as the 'tomographic Moho' (as defined in Diehl *et al.* 2009b). (a) absolute depth values of the 7.25 km/ s isolines for grid nodes matching the quality criteria (see section 4 of Supplementary Information for details on node selections and calculation). (b) The Moho map as in Spada *et al.* 2013, their fig. 11. (c) The absolute depth difference between the tomographic Moho (a) and the Moho map of Spada *et al.* (2013) for the same nodes as in (a). Nodes with no information in the Spada *et al.* (2013) model are reported as missing values and depicted as red crosses in (c). Dark grey tiles represent nodes with depth difference >16 km. The dark-red lines in both panels represent the major orogen fronts and fault systems that are displayed also in Fig. 1, in particular: AF, Alpine front; SAF, southern Alpine front; ApF, Apenninic front; DF, northwestern Dinarides front; PF, Periadriatic faults system.

gap in Moho information observed by different seismic methods, but they also support the previous findings and define the lateral extent of an anomalously high velocity in the lowermost crust that likely is the cause for all these observations with different seismic methods. Thus, we may conclude that the local Moho gap between the European and Adria crust–mantle boundaries is a real feature rather than an effect of illumination problems in different seismic experiments.

5.7 General remarks on LET interpretation and comparison with ANT models

The Ivrea body embedded within the Western Alpine orogen provides a prime example for the pivotal importance of a reliable model of the Moho topography consistent with the 3-D V_P and V_S structure of the crust for tectonic interpretations (e.g. Schmid *et al.* 2017 and references therein) and for seismotectonic studies (e.g. Malusà *et al.* 2017, and references therein). Obviously, no single seismic method applied to even a top-quality data set may allow to derive such a model. We may establish such a 3-D reference crustal model that may serve its purpose only by consistently combining highly reliable results from different seismic methods considering their specific strength and limitations.

In their ANT study, Qorbani *et al.* (2020) document difficulties to map topography of a deep first-order discontinuity like the Moho (their fig. 13) and this is method-inherent due to similarities in the kernels (e.g. Sadeghi-Bagherabadi *et al.* 2021, their fig. 6). At the same time though, ANT with data from a complete suite of periods provides prime information about the lateral V_S velocity variation (e.g. Soergel *et al.* 2022). Notably, sedimentary basins of large volume and significant amplitude velocity contrast are excellently resolved in their lateral dimensions. However, some vertical leakage to greater depth is similarly present in ANT as in LET (see Po plain or Molasse deepest trough in Molinari *et al.* 2020 and in our LET results (Fig. 6b, Supplementary Information Fig. S9).

6 CONCLUSION

In this study, we present a new 3-D seismic *P*-velocity tomographic model of the GAR (Hetény *et al.* 2018b)) obtained from the inversions of 24 yrs of local earthquake data. Three different catalogues and data sets were compiled and merged to create a uniform catalogue suitable for seismic tomography inversion. The three data sets are: (i) the one obtained from the latest regional tomography in the area of Diehl *et al.* (2009a), (ii) a newly reprocessed and repicked catalogue downloaded from EPOS-EMSC web services and (iii) the latest AARSC from Bagagli *et al.* (2022a). We repicked significant events reported in the EPOS-EMSC catalogue by applying the same approach as for the AARSC processing (Bagagli *et al.* 2022a), using the combination of the ADAPT repicking framework (Bagagli 2022b and c) and the VELEST software (Kissling 1988). The processing also provides uniform MLv magnitudes (Richter 1935; Hanka *et al.* 2010), which are consistent with the ones of the AARSC. The resulting continuous catalogue of ~12.5 yr of earthquake data for the GAR represents a unique data set to investigate the seismicity and crustal structure of the region. The update of the minimum 1-D V_P model and corresponding station delays for the GAR was a necessary step for quality filtering of the arrival-time data as well as to achieve a homogeneous set of hypocentres and an initial reference model for the 3-D LET inversion. The updated model is well comparable with previously published ones (Bagagli *et al.* 2022a, Braszus *et al.* 2024), documenting the high data quality.

A total of 1647 stations, 2286 events and 84326 ray paths (95% ray lengths > 34.62 km, Supporting Information Fig. S10) were used in the final LET 3-D inversion. In the well-resolved area (~5 °E–17 °E, ~42.5 °N–48.5 °N), a horizontal grid-node spacing of 20 km by 20 km and a vertical spacing of 7 to 15 km (increasing with depth) was used. Synthetic tests document the remarkably good amplitude recovery of the data set for most part of the study region. Our high-quality data set images the 3-D V_P structure of the GAR down to 60 km depth and compared to previous regional scale LET studies (e.g. Di Stefano *et al.* 2009; Diehl *et al.* 2009b), we extend the investigated region in the East from 12.5 °E to 17.0 °E and the North from 47.0 °N to 48.5 °N, thus extending the well-resolved region particularly in the Eastern Alps. Although our well-resolved area does not fully cover the complete GAR (Fig. 1), the new 3-D V_P model shows a large uniform resolution extent and presently denotes the widest crustal high-resolution passive LET investigation in the region. The results correlate well with previously known structures, yet they significantly extend our knowledge regarding areal coverage, precision and reliability. Thanks to the dense station network and the 24 yrs period of observation, the depth range of 25–50 km is nearly homogeneously well resolved and allows us to particularly well image the Moho.

First-order velocity anomalies like the Ivrea-body and the sedimentary foreland basins (i.e. Po Basin and Molasse Basin) are well resolved and evidence imaging reliability of regional structure within the crust. The *P*-velocity profiles sampled in Fig. 7 are in good agreement with the V_S results from previous ANT studies (Molinari *et al.* 2015; Soergel *et al.* 2022; Kaestle *et al.* 2024). The new LET-derived Moho map (7.25 km/s) provides an unprecedented densely sampled Moho topography across the region and where the information collocates, it agrees very well with previous studies (Diehl *et al.* 2009b; Spada *et al.* 2013; Michailos *et al.* 2023). The V_P model presented here may be used for crustal correction of receiver function analysis as well, even at smaller scales. Furthermore, the importance of a crustal reference model both for *P*- and *S*-body waves could bring significant benefits to further advance the understanding of the GAR region. This bold yet beneficial task of merging all models obtained in all CSS, RF, ANT and LET studies (including our new model) in a consistent approach is auspicious and worth pursuing. The comparisons of the Moho topography with previously published maps and of the new V_P model with 1-D V_S profiles from ANT studies at several key locations document the new LET results of combined 3-D V_P crustal velocities and Moho topography to be intrinsically consistent and reliable within the region of high resolution. Thus, the new LET results further improve our understanding of crustal structure geometries in the GAR, and they provide pivotal information for a future reference seismic 3-D crustal model of the region.

ACKNOWLEDGMENTS

The authors would like to thank the editor, Prof Huajian Yao. We also thank Erdinc Saygin and an anonymous reviewer for their constructive comments that helped improve this work. The AlpArray-Switzerland project is funded by the Swiss-AlpArray SINERGIA project CRSII2 154434/1 by Swiss National Science Foundation (SNSF). MB was supported by the European Union's research and innovation program under the Marie Sklodowska Curie Grant Agreement 101105516. MB thanks Camilla Rossi for the constant support and key scientific discussions. IM thanks the project Istituto Nazionale di Geofisica e Vulcanologia (INGV) Pianeta Dinamico 2023–2025 (Grant Number CUP D53J19000170001) supported by the Italian Ministry of University and Research ('Fondo finalizzato al rilancio degli investimenti delle amministrazioni centrali dello Stato e allo sviluppo del Paese, legge 145/2018') - Project MT_ADRIABRIDGE. The figures in this article have been generated using a newly developed, Python-based package *tomo2plt* (https://www.github.com/mbagagli/tomo2plt), that exploit Python and Matplotlib library (Hunter 2007) to handle SIMULPS outputs. The coastlines and national boundaries used in *tomo2plt* were retrieved from https://www.naturalearthdata.com. Fig. 1 was created using the Generic Mapping Tool (GMT; Wessel *et al.*, 1998) package. Most of the seismic data processing has been done using the ObsPy library (Beyreuther *et al.* 2010).

Author contribution: Conceptualization: all authors; Funding Acquisition and Resources: EK, IM, MB; Methodology: MB, EK, TD; Data Curation: MB, IM, EK; Investigation: all authors; Software: MB; Visualization: MB; Validation: EK, TD; Writing—original draft: EK, MB; Writing—review and editing: all authors.

SUPPORTING INFORMATION

Supplementary data are available at *GJIRAS* online.

Figure S1. Schematic workflow of the European-Mediterranean-Seismological-Center (EMSC) repicking. The output catalogue is then used together the Diehl et al. (2009a) and the Bagagli *et al.* (2022a) seismicity catalogue.

Figure S2. Original versus re-calculated local magnitude (MLv) of the 1108 events repicked from the EMSC bulletin for the time period May 2007–December 2015. The magnitudes are rounded to the first decimal and grouped for matches. Each dot colour represents the amount of pair occurrences for 2 given values.

Figure S3. Location error of the 774 well-resolved events of the AARSC catalogue (Bagagli *et al.* 2022a) in input to our tomography. The hypocentres' differences are calculated between the 1-D location of AARSC and the final location over the final 3-D VP tomographic model. This comparison provides us with an estimation of the average location error of our tomographic data set.

Figure S4. Resolution test for the final inversion data set at different damping values. These three values denote the optimal range of damping for the chosen 3-D gridding, the data set available and the apparent real velocity structure. The resolution within the RDE > 0.2 is rather uniform though not excellent considering the possible vertical leakage within the crust.

Figure S5. Results of resolution tests B using the 'synthetic-model' approach by Haslinger *et al.* (1999) are presented. The model, obtained over five iterations with a damping value of 70, is depicted through depth-slice overviews at various depths. To illustrate Vp anomalies, we use blue and red rectangles to represent high (+10 per cent) and low (−10 per cent) adjustments to the average Vp layer values, respectively. Earthquakes are highlighted by green circles, positioned within layers based on a specific range: from the node's depth minus half the distance to the preceding node to the node's depth plus half the distance to the preceding node. This positioning reflects the earthquakes that significantly influence each layer's results. The RDE contour of 0.2 is highlighted with a thick black line, while grey plus signs mark grid nodes. The average VP values are specified for each layer. Additionally, the GAR region, as defined by Hetényi *et al*. (2018b), is outlined in orange.

Figure S6. Results of resolution tests C using the 'synthetic-model' approach by Haslinger *et al.* (1999) are presented. The model, obtained over five iterations with a damping value of 70, is depicted through depth-slice overviews at various depths. To illustrate Vp anomalies, we use blue and red rectangles to represent high (+10 per cent) and low (−10 per cent) adjustments to the average Vp layer values, respectively. Earthquakes are highlighted by green circles, positioned within layers based on a specific range: from the node's depth minus half the distance to the preceding node to the node's depth plus half the distance to the preceding node. This positioning reflects the earthquakes that significantly influence each layer's results. The RDE contour of 0.2 is highlighted with a thick black line, while grey plus signs mark grid nodes. The average VP values are specified for each layer. Additionally, the GAR region, as defined by Hetényi *et al.* (2018b), is outlined in orange.

Figure S7. Bare tomographic result of 3-D Vp model depth-slices obtained using five iterations and a damping value of 70. The gray contour line represents the GAR region as defined by Hetényi *et al.* (2018b). The vP velocity structure is shown as a percentage change relative to the 1-D initial reference model. The thick black line corresponds to the RDE contour of 0.2. We define as 'well resolved' the regions above such value. Areas outside these contours are associated with fair or poor resolution.

Figure S8. Comparison of LET model by Virieux *et al.* (2023; their fig. S20) (top) and this study (bottom) along the CIFALPS transect that runs oblique across the Ivrea body and the Western Alpine arc. The white solid line denotes the European Moho and the black solid line the Adriatic Moho according to Spada *et al.* (2013). The purple line shows the Moho according to Michailos *et al.* (2023), obtained with receiver functions. Note the different colour scales where the bulk velocity of the Ivrea body (7 km/s) is shown in light blue in the top panel and in green in the bottom panel. While the large features in the two models are very similar and also correspond with the Moho topography by Spada *et al.* (2013), the large number of hypocentres in the upper crust and Ivrea body in combination with a smaller cell size (5 km x 5 km x 2 km) allow to resolve smaller structural features in the model of Virieux *et al.* (2023).

Figure S9. Comparison of AN model by Molinari *et al.* (2020, their fig. 9D) (top) and this LET study (bottom) along the EASI transect at ca. 13–13.5°E that runs from the Bohemian Massif to the Adriatic Sea (Hetényi 2018a). On the top panel, the isoline at Vs = 4.1 km/s is highlighted (grey dotted line) and several Mohos are plotted: Magrin & Rossi (2020) (black dashed line), Hetényi *et al.* (2018b) (orange line), Hrubcova & Geissier (2009) (yellow dot). The Spada *et al.* (2013) Moho—in darkredis highlighted in both panels. On the bottom panel, thick dashed black lines corresponding to the RDE contour of 0.2. Regions with RDE > 0.2 are considered well resolved. Areas outside these contours are associated with fair or poor resolution and are masked accordingly (masked with transparency).

Figure S10. Distribution of the ray-lengths used for the GAR final 3-D Vp LET tomography. The 95 per cent of lengths is > 34.62 km.

Table T1. Data set numbers in input to the relative data set calculations: (A) minimum 1-D and station delays calculations, and (B) 3-D tomography inversion calculation.

Table T2. Quality class scheme error. For each discrete classification, an absolute error interval (in seconds) and the relative per cent weight in the inversion procedure.

authors. Any queries (other than missing material) should be directed to the corresponding author for the paper.

CONFLICT OF INTEREST

The authors declare no conflicts of interest concerning the research, authorship and publication of this article.

DATA AVAILABILITY

The LET data set together with the 3-D *P*-wave velocity model, minimum 1-D *P*-wave velocity model, station delays, inventories and inversion traveltime data sets are stored here https://zenodo.org/records/14055284 in a permanent repository. In the same repository is uploaded the repicked EPOS-EMSC catalogue from May 2007 up to December 2015. The ADAPT framework code, the individual pickers (Bagagli 2019. 2021a, b) and the *tomo2plt* package used in the production of this work can be found at https://www.github.com/mbagagli.

REFERENCES

Ansorge, J., Mueller, S., Kissling, E., Guerra, I., Morelli, C. & Scarascia, S., 1979. Crustal section across the zone of Ivrea-Verbano from the Valais to the Lago Maggiore, *Boll. Geofis. Teor. Appl.,* **83,** 149–157.

Bagagli, M., 2019. filterpicker-python. Zenodo. https://doi.org/10.5281/zenodo.3609025.

Bagagli, M., 2021a. host-picker. Zenodo. https://doi.org/10.5281/zenodo.5579442.

Bagagli, M., 2021b. aurempickers. Zenodo. https://doi.org/10.5281/zenodo.5459631.

Bagagli, M., 2022b. *Seismicity and Seismic Tomography across Scales: Application to the Greater Alpine Region,* PhD Thesis, ETH Zurich.

Bagagli, M. 2022c. Adapt Framework. Zenodo. https://doi.org/10.5281/zenodo.6702855.

Bagagli, M., Molinari, I., Diehl, T., Kissling, E., Giardini, D. & Working Group, AlpArray, 2022a. The AlpArray Research seismicity-catalogue, *Geophys. J. Int.,* **231,** 921–943.

Behm, M., 2006. *2006: Accuracy and Resolution of a 3D Seismic Model of the Eastern Alps,* PhD thesis, The school of the thesis, Vienna University of Technology Vienna, Austria.

Behm, M., Brückl, E., Chwatal, W. & Thybo, H., 2007. Application of stacking and inversion techniques to three-dimensional wide-angle reflection and refraction seismic data of the Eastern Alps, *Geophys. J. Int.,* **170**(1), 275–298.

Beyreuther, M., Barsch, R., Krischer, L., Megies, T., Behr, Y. & Wassermann, J., 2010. ObsPy: a Python toolbox for seismology, *Seismol. Res. Lett.,* **81,** 530–533.

Bianchi, I., Behm, M., Rumpfhuber, E.M. & Bokelmann, G., 2015. A new seismic data set on the depth of the Moho in the Alps, *Pure appl. Geophys.,* **172,** 295–308.

Bianchi, I., Ruigrok, E., Obermann, A. & Kissling, E., 2021. Moho topography beneath the European Eastern Alps by global-phase seismic interferometry, *Solid Earth,* **12,** 1185–1196.

Bleibinhaus, F. & Gebrande, H., 2006. Crustal structure of the Eastern Alps along the TRANSALP profile from wide-angle seismic tomography, *Tectonophysics,* **414**(1-4), 51–69.

Blundell, D.J., Freeman, R., Mueller, S. & Button, S., 1992. *A Continent Revealed: The European Geotraverse, Structure and Dynamic Evolution*. Cambridge Univ. Press.

Braszus, B., Rietbrock, A., Haberland, C. & Ryberg, T. 2024. AI based 1-D P-and S-wave velocity models for the greater alpine region from local earthquake data, *Geophys. J. Int.,* **237**(2), 916–930.

Brückl, E. *et al.* 2007. Crustal structure due to collisional and escape tectonics in the Eastern Alps region based on profiles Alp01 and Alp02 from the ALP 2002 seismic experiment, *J. geophys. Res.,* **112,** B06308. https://doi.org/10.1029/2006JB004687.

Brun, J.-P. & Faccenna, C. 2008. Exhumation of high-pressure rocks driven by slab rollback, *Earth planet. Sci. Lett.,* **272,** 1–7.

Butler, R.W.H. 2013. Area balancing as a test of models for the deep structure of mountain belts, with specific reference to the Alps, *J. Struct. Geol.,* **52,** 2–16.

Carminati, E., Doglioni, C. & Scrocca, D. 2003. Apennines subduction-related subsidence of Venice (Italy), *Geophys. Res. Lett.,* **30**(13), 1717.

Chorowicz, J., 1970. La transversale de zrmanja (Yougoslavie), *Bull. Soc. Géolog. France,* **7,** 1028–1033.

Closs, H. & Labrouste, Y., 1963. *Seismologic Research in the Western Alps Employing the Large Explosions of 1956, 1958 and 1960 (in French)*. CNRS, pp. 241.

Csontos, L. & Nagymarosy, A., 1998. The Mid-Hungarian line: a zone of repeated tectonic inversions, *Tectonophysics,* **297,** 51–71.

D'Acquisto, M., Dal Zilio, L., Molinari, I., Kissling, E., Gerya, T. & van Dinther, Y., 2020. Tectonics and seismicity in the northern Apennines driven by slab retreat and lithospheric delamination, *Tectonophysics,* **789,** 228481.

Dezes, P. & Ziegler, P.A., 2002. Moho depth map of Western and Central Europe, *World Wide Web Address*: http://www.uni-bas.ch/eucor-urgent

Di Stefano, R., Bianchi, I., Ciaccio, M.G., Carrara, G. & Kissling, E., 2011. Three-dimensional Moho topography in Italy: new constraints from receiver functions and controlled source seismology, *Geochem. Geophys. Geosyst.,* **12,** 1–15.

Di Stefano, R., Kissling, E., Chiarabba, C., Amato, A. & Giardini, D., 2009. Shallow subduction beneath Italy: three-dimensional images of the Adriatic-European-tyrrhenian lithosphere system based on high-quality *P* wave arrival times, *J. geophys. Res.-Sol. Earth,* **114,** B05305. https://doi.org/10.1029/2008JB005641.

Diehl, T., Husen, S., Kissling, E. & Deichmann, N., 2009b. High-resolution 3-D *P*-wave model of the Alpine crust, *Geophys. J. Int.,* **179,** 1133–1147.

Diehl, T., Kissling, E., Herwegh, M. & Schmid, S.M., 2021. Improving absolute hypocenter accuracy with 3D Pg and Sg body-wave inversion procedures and application to earthquakes in the Central Alps region, *J. geophys. Res.: Solid Earth,* **126,** e2021JB022155.

Diehl, T., Kissling, E., Husen, S. & Aldersons, F., 2009a. Consistent phase picking for regional tomography models: application to the greater Alpine region, *Geophys. J. Int.,* **176,** 542–554.

Doglioni, C., Gueguen, E., Sàbat, F. & Fernandez, M., 1997. The Western Mediterranean extensional basins and the Alpine orogen, *Terra Nova,* **9,** 109–112.

Eberhart-Phillips, D., 1990. Three-dimensional *P* and *S* velocity structure in the Coalinga region, California, *J. geophys. Res.,* **95,** 15 343–315 363.

Edel, J., Fuchs, K., Gelbke, C. & Prodehl, C., 1975. Deep structure of the southern Rhinegraben area from seismic refraction investigations, *J. Geophys.,* **41,** 333–356.

Faccenna, C. *et al.*, 2014. Mantle dynamics in the Mediterranean, *Rev. Geophys.,* **52,** 283–332.

Faccenna, C., Piromallo, C., Crespo-Blanc, A., Jolivet, L. & Rossetti, F., 2004. Lateral slab deformation and the origin of the western Mediterranean arcs, *Tectonics,* **23,** 1–24.

Fantoni, R. & Franciosi, R., 2010. Tectono-sedimentary setting of the Po Plain and Adriatic foreland, *Rend. Fis. Acc. Lincei,* **21**(Suppl 1), S197–S209.

Frisch, W., 1979. Tectonic progradation and plate tectonic evolution of the Alps, *Tectonophysics,* **60,** 121–139.

Frost, E., Dolan, J., Sammis, C., Hacker, B., Cole, J. & Ratschbacher, L. 2009. Progressive strain localization in a major strike-slip fault exhumed from midseismogenic depths: structural observations from the Salzach-Ennstal-Mariazell-Puchberg fault system, Austria, *J. geophys. Res.: Solid Earth,* **114**(B4), Wiley Online Library. https://doi.org/10.1029/2008JB005763.

Fry, B., Deschamps, F., Kissling, E., Stehly, L. & Giardini, D. 2010. Layered azimuthal anisotropy of Rayleigh wave phase velocities in the European Alpine lithosphere inferred from ambient noise, *Earth planet. Sci. Lett.,* **297**(1–2), 95–102.

Grad, M., Tiira, T. & ESC Working Group, 2009. The Moho depth map of the European Plate, *Geophys. J. Int.,* **176**(1), 279–292.

Grützner, C. *et al.* 2021. Holocene surface-rupturing earthquakes on the Dinaric Fault System, western Slovenia, *Solid Earth,* **12,** 2211–2234.

Guterch, A. *et al.* 2003. CELEBRATION 2000 seismic experiment, *Stud. Geophys. Geod.,* **47**(3), 659–669.

Haas, J., Kovács, S., Krystyn, L. & Lein, R., 1995. Significance of late Permian-Triassic Facies zones in terrane reconstructions in the Alpine-North Pannonian domain, *Tectonophysics,* **242,** 19–40.

Handy, M.R., Schmid, S.M., Bousquet, R., Kissling, E. & Bernoulli, D., 2010. Reconciling plate-tectonic reconstructions of Alpine Tethys with the geological–geophysical record of spreading and subduction in the Alps, *Earth Sci. Rev.,* **102,** 121–158.

Handy, M.R., Ustaszewski, K. & Kissling, E., 2015. Reconstructing the Alps—Carpathians—Dinarides as a key to understanding switches in subduction polarity, slab gaps and surface motion, *Int. J. Earth Sci. (Geol. Rundsch),* **104,** 1–26.

Hanka, W., Saul, J., Weber, B., Becker, J., Harjadi, P. & Fauzi, GITEWS Seismology Group, 2010. Real-time earthquake monitoring for tsunami warning in the Indian Ocean and beyond, *Nat. Haz. Earth Syst. Sci.,* **10,** 2611–2622.

Haslinger, F. & Kissling, E., 2001. Investigating effects of 3-D ray tracing methods in local earthquake tomography, *Phys. Earth planet. Inter.,* **123,** 103–114.

Haslinger, F. *et al.* 1999. 3D crustal structure from local earthquake tomography around the Gulf of Arta region, NW Greece, *Tectonophysics,* **304,** 201–218.

Herwegh, M. *et al.* 2019. Late stages of continent-continent collision: timing, kinematic evolution, and exhumation of the Northern rim (Aar Massif) of the Alps, *Earth Sci. Rev.,* **200,** 102959. https://doi.org/10.1016/j.earscirev.2019.102959.⟨0:pub-id 0:pub-id-type="doi"⟩10.1016/j.earscirev.2019.102959⟨/0:pub-id⟩

Hetényi, G. *et al.* 2018b. The AlpArray Seismic Network—a large-scale European experiment to image the Alpine orogen, *Surv. Geophys.,* **39,** 1009–1033.

Hetényi, G., Plomerová, J., Bianchi, I., Kampfová Exnerová, H., Bokelmann, G., Handy, M.R. & Babuška, V., 2018a. From mountain summits to roots: crustal structure of the Eastern Alps and Bohemian Massif along longitude 13.3° E, *Tectonophysics,* **744,** 239–255.

Hinsch, R., 2013. Laterally varying structure and kinematics of the Molasse fold and thrust belt of the Central Eastern Alps: implications for exploration, *AAPG Bull.,* **97,** 1805–1831.

Holliger, K. & Kissling, E., 1992. Gravity interpretation of a unified 2-D acoustic image of the central Alpine collision zone, *Geophys. J. Int.,* **111,** 213–225.

Hrubcová, P. & Geissler, W.H., 2009. The crust-mantle transition and the Moho beneath the Vogtland/West Bohemian region in the light of different seismic methods, *Stud. Geophys. Geod.,* **53,** 275–294.

Hrubcová, P., Środa, P., Grad, M., Geissler, W.H., Guterch, A., Vozár, J. & Hegedűs, E., 2010. From the Variscan to the Alpine Orogeny: crustal structure of the Bohemian Massif and the Western Carpathians in the light of the SUDETES 2003 seismic data, *Geophys. J. Int.,* **183**(2), 611–633.

Hrubcová, P., Środa, P., Špičák, A., Guterch, A., Grad, M., Keller, G.R., Brueckl, E. & Thybo, H., 2005. Crustal and uppermost mantle structure of the Bohemian Massif based on CELEBRATION 2000 data, *J. geophys. Res.,* **110,** B11305. https://doi.org/10.1029/2004JB003080.

Hunter, J.D., 2007. Matplotlib: a 2D graphics environment, in *Computing in Science & Engineering,* **9,** pp. 90–95, IEEE Computer Society.

Husen, S., Diehl, T. & Kissling, E., 2009. The effects of data quality in local earthquake tomography: application to the Alpine region, *Geophysics,* **74**(6), WCB71–WCB79.

Jolivet, L., Faccenna, C. & Piromallo, C., 2009. From mantle to crust: stretching the Mediterranean, *Earth planet. Sci. Lett.,* **285**(1–2), 198–209.

Jolivet, L., Faccenna, C., Goffé, B., Burov, E. & Agard, P., 2003. Subduction tectonics and exhumation of high-pressure metamorphic rocks in the Mediterranean orogens, *Am. J. Sci.,* **303,** 353–409.

Kaestle, E.D., Tilmann, F. & AlpArray and Swath-D Working Groups, 2024. Anisotropic reversible-jump McMC shear velocity tomography of the eastern Alpine crust, *Geochem. Geophys. Geosyst.,* **25,** e2023GC011238.

Kaestle, E.D. *et al.* 2018. Surface wave tomography of the Alps using ambient-noise and earthquake phase velocity measurements, *J. geophys. Res.: Solid Earth,* **123,** 1770–1792.

Kaestle, E.D., Rosenberg, C., Boschi, L., Bellahsen, N., Meier, T. & El-Sharkawy, A. 2020. Slab break-offs in the Alpine subduction zone, *Int. J. Earth Sci. (Geol. Rundsch.),* **109,** 587–603.

Kapuralič, J., Sumanovac, F. & Markusic, S. 2019. Crustal structure of the northern Dinarides and southwestern part of the Pannonian basin inferred from local earthquake tomography, *Swiss J. Geosci.,* **112,** 181–198.

Kissling, E. & Schlunegger, F. 2018. Rollback orogeny model for the evolution of the Swiss Alps, *Tectonics,* **37,** 1097–1115.

Kissling, E. 1988. Geotomography with local earthquake data, *Rev. Geophys.,* **26,** 659–698.

Kissling, E., Ellsworth, W.L., Eberhart-Phillips, D. & Kradolfer, U. 1994. Initial reference models in local earthquake tomography, *J. geophys. Res.: Solid Earth,* **99,** 19635–19646.

Kissling, E., Husen, S. & Haslinger, F. 2001. Model parametrization in seismic tomography: a choice of consequence for the solution quality, *Phys. Earth planet. Inter.,* **123,** 89–101.

Kissling, E., Schmid, S.M., Lippitsch, R., Ansorge, J. & Fügenschuh, B., 2006. Lithosphere structure and tectonic evolution of the Alpine arc: new evidence from high-resolution teleseismic tomography, *Geol. Soc. London Mem.,* **32**(1), 129–145.

Lanza, R. 1982. Models for interpretation of the magnetic anomaly of the Ivrea body, *Geol. Alpine,* **58,** 85–94.

Lee, T., Diehl, T., Kissling, E. & Wiemer, S., 2023. New insights into the Rhône–Simplon fault system (Swiss Alps) from a consistent earthquake catalogue covering 35 yr, *Geophys. J. Int.,* **232**(3), 1568–1589.

Lenhardt, WA, Švancara, J, Melichar, PE, Pazdírková, J, Havír, J & Sýkorová, Z., 2007. Seismic activity of the Alpine-Carpathian-Bohemian Massif region with regard to geological and potential field data, *Geologica Carpathica,* **58**(4), 397–412.

Lippitsch, R., Kissling, E. & Ansorge, J. 2003. Upper mantle structure beneath the Alpine orogen from high-resolution teleseismic tomography, *J. geophys. Res.: Solid Earth,* **108,** 108. https://doi.org/10.1029/2002JB002016.

Lu, Y., Stehly, L., Paul, A. & Group, A.W. 2018. High-resolution surface wave tomography of the European crust and uppermost mantle from ambient seismic noise, *Geophys. J. Int.,* **214,** 1136–1150.

Magrin, A. & Rossi, G. 2020. Deriving a new crustal model of Northern Adria: the Northern Adria Crust (NAC) model, *Front. Earth Sci.,* **8,** 89.

Malusà, M.G., Zhao, L., Eva, E., Solarino, S., Paul, A., Guillot, S., Schwartz, S., *et al.* 2017 Earthquakes in the western Alpine mantle wedge, *Gondwana Research,* **44,** 89–95.

Menichelli, I., De Gori, P., Lucente, F.P., Improta, L. & Chiarabba, C. 2023. Lithosphere structure, processes, and physical State of the Alpine-Apennine system, *J. geophys. Res.: Solid Earth,* **128,** e2023JB026411.

Michailos, K. *et al.* 2023. Moho depths beneath the European Alps: a homogeneously processed map and receiver functions database, *Earth Syst. Sci. Data Discuss.,* **2023,** 1–32.

Mitterbauer, U. *et al.* 2011. Shape and origin of the East-Alp slab constrained by the ALPASS teleseismic model, *Tectonophysics,* **510,** 195–206.

Molinari, I. & Morelli, A. 2011. EPcrust: a reference crustal model for the European plate, *Geophys. J. Int.,* **185**(1), 352–364.

Molinari, I., Obermann, A., Kissling, E., Hetényi, G., Boschi, L. & the AlpArray-EASI Working Group, 2020. 3D crustal structure of the Eastern Alpine region from ambient noise tomography, *Results Geophys. Sci.,* **1,** 100006.

Molinari, I., Verbeke, J., Boschi, L., Kissling, E. & Morelli, A. 2015. Italian and Alpine three-dimensional crustal structure imaged by ambient-noise surface-wave dispersion, *Geochem. Geophys. Geosyst.,* **16,** 4405–4421.

Mooney, W.D., Barrera-Lopez, C., Suarez, M.G. & Castelblanco, M.A. 2023. Earth crustal Model 1 (ECM1): a 1° x 1° global seismic and density model, *Earth Sci. Rev.,* **243,** 104493.

Mooney, W.D., Prodehl, C. & Pavlenkova, N.I. 2002. Seismic velocity structure of the continental lithosphere from controlled source data, in *International Geophysics Series (Vol. 81),* pp. 887–910, eds Lee, W.H.K., Kanamori, H., Jennings, P.C. & Kisslinger, C., Elsevier.

Mroczek, S., Tilmann, F., Pleuger, J., Yuan, X. & Heit, B. 2023. Investigating the eastern Alpine–Dinaric transition with teleseismic receiver functions: evidence for subducted European crust, *Earth planet. Sci. Lett.,* **609,** 118096.

Mueller, S. 1977. *A New Model of the Continental Crust*. *Geophysical Monograph*, **20,** American Geophysical Union, 289–317.

Mueller, S., Ansorge, J., Egloff, R. & Kissling, E. 1980. A crustal cross-section along the Swiss Geotraverse from the Rhinegraben to the Po plane, *Eclogae geol. Helv.,* **73**(2), 463–485.

Najafabadi, A.J., Haberland, C., Le Breton, E., Handy, M.R., Verwater, V.F., Heit, B. & Weber, M. 2022. Constraints on crustal structure in the vicinity of the Adriatic Indenter (European Alps) from VP and VP/vs local earthquake tomography, *J. geophys. Res.: Solid Earth,* **127**(2), e2021JB023160.

Nouibat, A., Stehly, L., Paul, A., Schwartz, S., Bodin, T., Dumont, T., Rolland, Y. & Brossier, R., Cifalps Team and AlpArray Working Group. 2022. Lithospheric transdimensional ambient-noise tomography of W-Europe: implications for crustal-scale geometry of the W-Alps, *Geophys. J. Int.,* **229,** 862–879.

Ortner, H., Aichholzer, S., Zerlauth, M., Pilser, R. & Fügenschuh, B. 2015. Geometry, amount, and sequence of thrusting in the Subalpine Molasse of western Austria and southern Germany, *Tectonics,* **34,** 1–30.

Paffrath, M., Friederich, W., Schmid, S.M., Handy, M.R. & the AlpArray and AlpArray-Swath D Working Group, 2021. Imaging structure and geometry of slabs in the greater Alpine area—a *P*-wave travel-time tomography using AlpArray Seismic Network data, *Solid Earth,* **12,** 2671–2702.

Paul, A. 2022. What we (possibly) know about the 3-D structure of crust and mantle beneath the Alpine chain. Available at: https://hal.archives-ouvertes.fr/hal-03747864.

Paul, A., Cattaneo, M., Thouvenot, F., Spallarossa, D., Béthoux, N. & Frechet, J. 2001. A three-dimensional crustal velocity model of the south-western Alps from local earthquake tomography, *J. geophys. Res.: Solid Earth,* **106**(B9), 19 367–19 389.

Pezzo, G. *et al.* 2020. Active fold-thrust belt to foreland transition in northern Adria, Italy, tracked by seismic reflection profiles and GPS offshore data, *Tectonics,* **39,** e2020TC006425.

Pieri, M. & Groppi, G. 1981. Subsurface geological structure of the Po Plain, Prog. Fin.Geodinamica, sottoprog. Modelle Strutturale 13, Rome. CNR Publ. 414, 1–11.

Pistone, M., Ziberna, L., Hetényi, G., Scarponi, M., Zanetti, A. & Müntener, O. 2020. Joint geophysical-petrological modeling on the Ivrea geophysical body beneath Valsesia, Italy: constraints on the continental lower crust, *Geochem. Geophys. Geosyst.,* **21,** e2020GC009397.

Plomerová, J., Žlebcíková, H., Hetényi, G., Vecsey, L., Babuška, V. & AlpArray-EASI and AlpArray working groups, 2022. Two subduction-related heterogeneities beneath the Eastern Alps and the Bohemian Massif imaged by high-resolution *P*-wave tomography, *Solid Earth,* **13,** 251–270.

Prodehl, C. & Mooney, W.D. 2012. *Exploring the Earth's Crust: History and Results of Controlled-source Seismology, Memoir /Geological Society of America (Vol. 208)*. Geological Society of America.

Qorbani, E., Zigone, D., Handy, M.R., Bokelmann, G. & AlpArray-EASI Working Group, 2020. Crustal structures beneath the Eastern and Southern Alps from ambient noise tomography, *Solid Earth,* **11**(5), 1947–1968.

Rajh, G., Stipčević, J., Živčić, M., Herak, M., Gosar, A. & the AlpArray Working Group, 2022. One-dimensional velocity structure modeling of the Earth's crust in the northwestern Dinarides, *Solid Earth,* **13,** 177–203.

Rajh, G., Stipčević, J., Živčić, M., Herak, M., Gosar, A. & Group, T.A.W. 2024. *Investigation of the Upper Crustal Structure in the NW Dinarides Using Local Earthquake Tomography,* ESSOAR. https://doi.org/10.22541/essoar.171838389.91461123/v1.

Reiter, F., Ortner, H. & Brandner, R. 2003. Seismically active Inntal fault zone: inverted European rift structures control upper plate deformation, *Mem. Sci. Geol* **54,** 233–234.

Richter, C.F. 1935. An instrumental earthquake magnitude scale, *Bull. seism. Soc. Am.,* **25,** 1–32. The Seismological Society of America.

Rivalenti, G., Garuti, G. & Rossi, A. 1975. The origin of the Ivrea-Verbano basic formation (Western Italian Alps)—whole rock geochemistry, *Boll. Soc. Geol. Ital.,* **94,** 1149–1186.

Rojo Limón, G., Kissling, E., Ouillon, G. & Sornette, D. 2021. A consistent and high-quality M4+ earthquake catalogue for Turkey 2007–2016 from two independent catalogues, *Geophys. J. Int.,* **225,** 711–728.

Rosenberg, C.L. *et al.* 2018. Relating collisional kinematics to exhumation processes in the Eastern Alps, *Earth Sci. Rev.,* **176,** 311–344.

Rosenberg, C.L., Berger, A., Bellahsen, N. & Bousquet, R. 2015. Relating orogen width to shortening, erosion, and exhumation during Alpine collision, *Tectonics,* **34,** 1306–1328.

Rosenberg, C.L. & Schneider, S. 2008. The western termination of the SEMP Fault (eastern Alps) and its bearing on the exhumation of the Tauern Window, *Geol. Soc. Lond. Spec. Publ.,* **298,** 197–218. Geological Society of London.

Roure, F., Polino, R. & Nicolich, R. 1990. Early Neogene deformation beneath the Po plain: constraints on the post-collisional Alpine evolution, *Mém. Soc. géolog. France (1833),* **156,** 309–321.

Royden, L.H. & Burchfiel, B.C. 1989. Are systematic variations in thrust belt style related to plate boundary processes? (The western Alps versus the Carpathians), *Tectonics,* **8**(1), 51–61.

Sadeghi-Bagherabadi, A., Vuan, A., Aoudia, A. & Parolai, S., the AlpArray and Swath-D Working Groups, 2021. High-resolution crustal Swave velocity model and Moho geometry beneath the Southeastern Alps: new insights from the SWATH-D experiment, *Front. Earth Sci.,* **9,** 641113. https://doi.org/10.3389/feart.2021.641113.

Scarponi, M., Kvapil, J., Plomerová, J., Solarino, S. & Hetényi, G. 2024. New constraints on the shear wave velocity structure of the Ivrea geophysical body from seismic ambient noise tomography (Ivrea-Verbano Zone, Alps), *Geophys. J. Int.,* **236**(2), 1089–1105.

Schlunegger, F. & Kissling, E., 2015. Slab rollback orogeny in the Alps and evolution of the Swiss Molasse basin, *Nat. Commun.,* **6**(1), 8605.

Schmid, S.M. & Kissling, E. 2000. The arc of the western Alps in the light of geophysical data on deep crustal structure, *Tectonics,* **19,** 62–85.

Schmid, S.M. *et al.* 2008. The Alpine–Carpathian–Dinaridic Orogenic system: correlation and evolution of tectonic units, *Swiss J. Geosci.,* **101,** 139–183.

Schmid, S.M., Fügenschuh, B., Kissling, E. & Schuster, R. 2004. Tectonic map and overall architecture of the Alpine orogen, *Eclogae Geol. Helv.,* **97,** 93–117.

Schmid, S.M., Kissling, E., Diehl, T., van Hinsbergen, D.J. & Molli, G. 2017. Ivrea mantle wedge, arc of the Western Alps, and kinematic evolution of the Alps–Apennines orogenic system, *Swiss J. Geosci.,* **110,** 581–612.

Schmid, S.M., Pfiffner, O.A., Froitzheim, N., Schoenborn, G. & Kissling, E. 1996. Geophysical–geological transect and tectonic evolution of the Swiss–Italian Alps, *Tectonics,* **15,** 1036–1064.

Schmid, S.M., Scharf, A., Handy, M.R. & Rosenberg, C.L. 2013. The Tauern Window (Eastern Alps. Austria): a new tectonic map, with cross sections and a tectonometamorphic synthesis, *Swiss J. Geosci.,* **106,** 1–32.

Soergel, D., Pedersen, H.A., Bodin, T., Paul, A., Stehly, L. & the AlpArray Working Group, 2022. Bayesian analysis of azimuthal anisotropy in the Alpine lithosphere from beamforming of ambient noise cross-correlations, *Geophys. J. Int.,* **232**(1), 429–450.

Solarino, S. *et al.* 2018. Mantle wedge exhumation beneath the Dora-Maira (U)HP dome unravelled by local earthquake tomography (Western Alps), *Lithos,* **296–299,** 623–636.

Solarino, S., Kissling, E., Sellami, S., Smriglio, G., Thouvenot, F., Granet, M., Bonjer, K.P. & Slejko, D. 1997. Compilation of a recent seismicity data base of the greater Alpine region from several seismological networks and preliminary 3D tomographic results, Annali di Geofisica. **XL,** 161–174. Retrieved fromhttps://www.earth-prints.org/handle/2122/1542

Spada, M., Bianchi, I., Kissling, E., Agostinetti, N.P. & Wiemer, S., 2013. Combining controlled-source seismology and receiver function information to derive 3-D Moho topography for Italy, *Geophys. J. Int.,* **194,** 1050–1068.

Spakman, W. & Wortel, M.J.R. 2004. A tomographic view on Western Mediterranean geodynamics, Chapter 2in *The Transmed Atlas—The Mediterranean Region from Crust to Mantle,* pp. 31–52, eds Cavazza, W., Roure, F. M., Stampfli, G. M. & Ziegler, P. A., Springer.

Stehly, L., Fry, B., Campillo, M., Shapiro, N.M., Guilbert, J., Boschi, L. & Giardini, D., 2009. Tomography of the Alpine region from observations of seismic ambient noise, *Geophys. J. Int.,* **178,** 338–350.

Sternai, P., Jolivet, L., Menant, A. & Gerya, T. 2014. Driving the upper plate surface deformation by slab rollback and mantle flow, *Earth planet. Sci. Lett.,* **405,** 110–118.

Stipcevic, J., Herak, M., Molinari, I., Dasovic, I., Tkalcic, H. & Gosar, A. 2020. Crustal thickness beneath the Dinarides and surrounding areas from receiver functions, *Tectonics,* **39**(3), e2019TC005872.

Sumanovac, F., Oreskovic, J., Grad, M. & ALP2002 Working Group, 2009. Crustal structure at the contact of the Dinarides and Pannonian basin based on 2-D seismic and gravity interpretation of the Alp07 profile in the ALP experiment, *Geophys. J. Int.,* **179,** 615–633.

Szwillus, W., Afonso, J.C.C., Ebbing, J. & Mooney, W.D. 2019. Global crustal thickness and velocity structure from geostatistical analysis of seismic data, *J. geophys. Res.: Solid Earth,* **124,** 1626–1652.

Thurber, C.H., 1983. Earthquake locations and three-dimensional crustal structure in the Coyote Lake area, central California, *J. geophys. Res.: Solid Earth,* **88,** 8226–8236.

Tricart, P. 1984. From passive margin to continental collision; a tectonic scenario for the Western Alps, *Am. J. Sci.,* **284,** 97–120.

Trümpy, R. 1960. Paleotectonic evolution of the Central and Western Alps, *Geol. Soc. Am. Bull.,* **71,** 843–907.

Ustaszewski, K., Schmid, S.M., Fügenschuh, B., Tischler, M., Kissling, E. & Spakman, W. 2008. A map-view restoration of the Alpine-Carpathian-Dinaridic system for the early Miocene, *Swiss J. Geosci.,* **101,** 273–294.

Virieux, J., Paul, A., Langlais, M., Janex, G., Gueguen, P., Helmstetter, A. & Stehly, L., 2023. Assessing the reliability of local earthquake tomography for crustal imaging: 30 yr of records in the Western Alps as a case study, *Geophys. J. Int.,* **236**(1), 99–118.

Wagner, M., Kissling, E. & Husen, S., 2012. Combining controlled-source seismology and local earthquake tomography to derive a 3-D crustal model of the western Alpine region: combined 3-D crustal model of the western Alps, *Geophys. J. Int.,* **191,** 789–802.

Waldhauser, F., Kissling, E., Ansorge, J. & Mueller, S. 1998. Three-dimensional interface modelling with two-dimensional seismic data: the Alpine crust–mantle boundary, *Geophys. J. Int.,* **135,** 264–278.

Wessel, P. & Smith, W.H.F. 1998. New, improved version of generic mapping tools released, *EOS, Trans. Am. geophys. Un.,* **79,** 579–579.

Ye, S., Ansorge, J., Kissling, E. & Mueller, S. 1995. Crustal structure beneath the Swiss Alps derived from seismic refraction data, *Tectonophysics,* **242,** 199–221.

Zhao, L. *et al.* 2016. Continuity of the Alpine slab unraveled by high-resolution *P* wave tomography, *J. geophys. Res. Solid Earth,* **121,** 8720–8737.

Zhao, L. *et al.* 2020. Evidence for a serpentinized plate interface favouring continental subduction, *Nat. Commun.,* **11,** 2171.